

OKINAWA INSTITUTE OF SCIENCE AND TECHNOLOGY
GRADUATE UNIVERSITY

Thesis submitted for the degree

Doctor of Philosophy

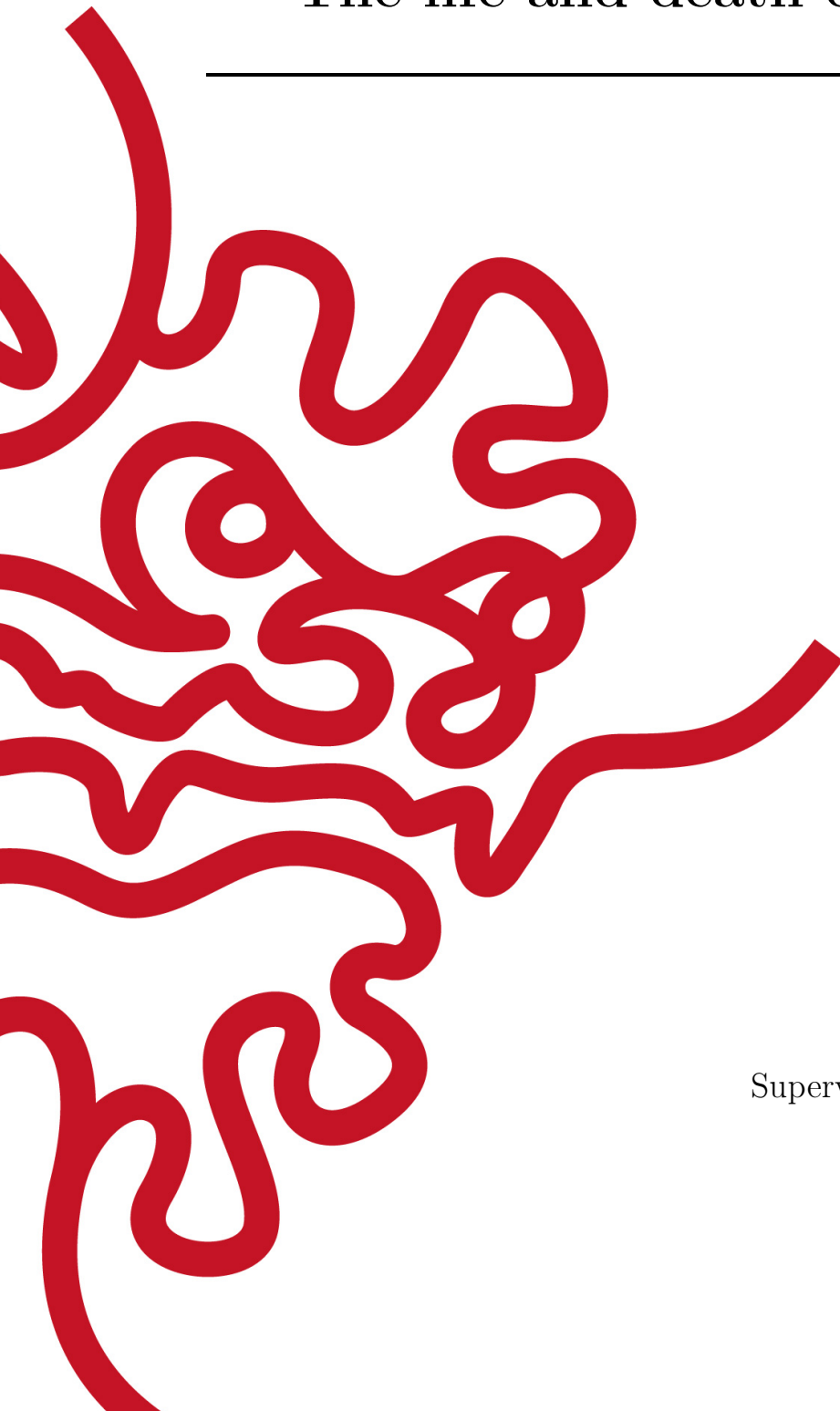
The life and death of vortex 161

by

Lee James O’Riordan

Supervisor: **Prof. Thomas Busch**

September, 2016



Declaration of Original and Sole Authorship

I, Lee James O’Riordan, declare that this thesis entitled *The life and death of vortex 161* and the data presented in it are original and my own work.

I confirm that:

- This work was done solely while a candidate for the research degree at the Okinawa Institute of Science and Technology Graduate University, Japan.
- No part of this work has previously been submitted for a degree at this or any other university.
- References to the work of others have been clearly attributed. Quotations from the work of others have been clearly indicated, and attributed to them.
- In cases where others have contributed to part of this work, such contribution has been clearly acknowledged and distinguished from my own work.
- None of this work has been previously published elsewhere, with the exception of the following: (provide list of publications or presentations, or delete this part). (If the work of any co-authors appears in this thesis, authorization such as a release or signed waiver from all affected co-authors must be obtained prior to publishing the thesis. If so, attach copies of this authorization to your initial and final submitted versions, as a separate document for retention by the Graduate School, and indicate on this page that such authorization has been obtained).

Date: September, 2016

Signature:

Abstract

The life and death of vortex 161

Maximum 400 words, not to exceed one A4 page.

No figures or tables. No references. Just aims, brief methods, results, brief conclusions.

Avoid over-detailed technical method descriptions.

Should be readable to a literate science reader familiar with your general area, but not necessarily experts-only material

This will be published online within 3 months of award of the degree, as a minimum. The entire thesis must be published within one year, unless restrictions apply (as above).

Acknowledgment

Theses must acknowledge assistance received in any of the following areas:

- Designing the research
- Executing the research
- Analyzing the data
- Interpreting the data/research
- Writing, proofing, or copyediting the manuscript

Where co-authors have contributed to papers arising from the work, you should not include their data unless it is essential for the scientific narrative. In such cases, full disclosure of the contribution is required. Acknowledge any work performed by others, whether at OIST or outside OIST.

Abbreviations

All abbreviations used in the thesis should be listed here, with their definitions, in alphabetical order. This includes trivial and commonly used abbreviations (at your own discretion), but not words that have entered into general English usage (such as laser or DNA). In particular, non-standard abbreviations should be presented here. This is an aid to the reader who may not read all sections of the thesis.

PPT	positive partial transpose
SRPT	Schrödinger-Robertson partial transpose

Glossary

Chemical potential	Energy to overcome for adding an atom to the system
--------------------	---

Nomenclature

h	Planck constant ($6.626\,070\,04 \times 10^{-34}$ Js).
\hbar	Planck constant over 2π ($1.054\,572\,66 \times 10^{-34}$ Js).
L_z	Angular momentum operator along the z -dimension; $xp_y - yp_x$.
∇	Gradient operator.
Ω	Angular rotation frequency of condensate.
ξ	Condensate healing length; the distance from a region of zero density at vortex core to bulk density.
μ	Chemical potential of the condensate; the energy change per unit change in particle number.

If desired, an optional and short dedication may be
included here.

Contents

Declaration of Original and Sole Authorship	iii
Abstract	v
Acknowledgment	vii
Abbreviations	ix
Glossary	xi
Nomenclature	xiii
Contents	xvii
List of Figures	xix
List of Tables	xxiii
 Introduction	 1
1 Literature review	3
1.1 Cold atoms	3
1.1.1 Cooling of atomic gases	3
1.1.2 Introduction to Bose–Einstein condensation	4
1.1.3 Theoretical description of BECs: Gross–Pitaevskii equation . . .	6
1.1.4 Realisation of Bose–Einstein condensation in dilute gases	8
1.1.5 Lower dimensional condensates	9
1.2 Superfluidity	10
1.2.1 Introduction to superfluidity	10
1.2.2 Vortices in Bose–Einstein condensates	12
1.2.3 Vortex lattices	14
1.2.4 Fast rotation limit	15
1.2.5 Optical lattice potentials	18
1.2.6 Recent advances and discoveries	20

2	Numerics	21
2.1	Numerics	21
2.2	Angular momentum operators using FSO method	23
2.2.1	Time evolution	23
2.3	Vortex tracking	25
2.4	General purpose GPU computing	25
2.5	GPUE: GPU Gross–Pitaevskii equation solver	26
2.5.1	Introduction	27
2.5.2	Coherent Tunnelling by Adiabatic Passage	29
2.5.3	Atom Chips	30
2.5.4	MPI and CUDA	34
2.5.5	3D Simulations	35
2.5.6	Conclusions	37
2.5.7	Acknowledgements	38
3	Vortex dynamics	41
3.1	Vortex lattice	41
4	Moiré superlattice structures	43
4.1	Delta-kick dynamics	43
4.2	Dynamics following a kick	46
4.2.1	Non-rotating condensate	46
4.2.2	Rapidly rotating condensate	47
4.3	Kinetic energy decomposition	49
4.4	Superlattice structures	49
4.5	Moiré interference theory	49
5	Defect engineering	51
5.0.1	Rapidly rotating BEC	51
5.0.2	Order/disorder	51
5.0.3	Phase imprinting defects	52
5.0.4	Things to note	53
5.0.5	Correlations	54
5.0.6	Numerics and results	54
	Conclusion	57
	A Appendices and Supplementary Data	59
	Bibliography	61

List of Figures

2.1	A single pass through the Fourier split-operator method.	22
2.2	Simplified combined sequence and state diagram for GPUE operation. .	28
2.3	(Color online) Schematic of the suggested setup for observing the CTAP process in a system of waveguides. Note that the asymmetric approach of the outer wires to the middle wire is exaggerated, so that the counter-intuitive arrangement is visible. The atom is initially located in the left guide and, due to the presence of a harmonic oscillator potential V_z in the z -direction, travels along the direction indicated by the red solid arrow. We also show the expected position of the atom at $t = \pi/\omega_z$ in the right hand side guide and indicate the orientation of the bias field, B_b , and the applied field, B_{ip} (purple dashed arrows).	29
2.4	(Color online) Isosurfaces of the waveguides created on an atom chip with the direction of propagation indicated by the blue solid arrow (for clarity $V_z = 0$ in this plot). The dimensions of the interesting area on the chip we simulate are $20\mu\text{m} \times 1000\mu\text{m}$ ($x \times z$) and we take a height (y direction) above the chip of $4\mu\text{m}$ into account. The three wires are initially equally separated by $7\mu\text{m}$ and their distance at the position of closest approach is $4.3\mu\text{m}$. The left wire remains straight initially for a distance of $50\mu\text{m}$, which produces an asymmetry in the point of closest approach of the left and right wires to the middle wire as indicated by ξ . The bias and applied fields (indicated by the green dashed arrows) are $B_b = 140 \times 10^{-4}\text{T}$ and $B_{ip} = 300 \times 10^{-4}\text{T}$. In (a) the currents of the left, middle and right wires are $I_L = I_M = I_R = 0.1\text{A}$ respectively and in (b) the currents of the left and right wires are $I_L = I_R = 0.1\text{A}$ and the middle wire current is reduced to $I_M = 0.07\text{A}$	32
2.5	(Color online) Contour plot of the waveguides at $500\mu\text{m}$ along the z -axis. Panel (a) shows the deformation of the waveguides when all currents are equal, $I_L = I_M = I_R = 0.1\text{A}$ and panel (b) shows how this effect can be mitigated by using a reduced middle wire current of $I_M = 0.07\text{A}$, while the current in the outer wires remain at $I_L = I_R = 0.1\text{A}$	33
2.6	(Color online) The population in the left (blue dashed line), middle (green dot-dash line) and right (red solid line) waveguides as a function of time for (a) the counter-intuitive waveguide arrangement and (b) for intuitive, direct tunnelling one. The current in the middle wire is reduced to $I_M = 0.07\text{A}$	39

2.7	(Color online) The density of the atomic state at $t = 0.048$ for (a) the counter-intuitive setup and (b) the intuitive one. The current in the middle wire is $I_M = 0.07$ A in both cases.	40
2.8	(Color online) The final population in the target waveguide for both the CTAP (red solid line) and intuitive (blue dashed line) processes, for values of $I_M = 0.0672$ A to $I_M = 0.0761$ A in steps of 0.001 A.	40
4.1	(a) Vortex lattice ground-state in a harmonic trap with $\omega_{\perp} = 2\pi$ s ⁻¹ and rotating at $\Omega = 0.995\omega_{\perp}$. This plot shows a condensate with a diameter of approximately 580 μ m; (b) Zoom in of vortex lattice at central density; (c) Optical lattice potential with a periodicity matching that of the vortex lattice.	44
4.2	Compressible energy spectrum of a non-rotating condensate directly following a kick. A peak at $k = 4\pi/(\sqrt{3}a_o)$ can be seen, which corresponds to the lattice spacing, a_o (indicated by the dashed line), and the smaller, higher energy peaks can be attributed to higher harmonics between nearest and next-nearest neighbours.	46
4.3	(a) Main peak of the compressible kinetic energy spectrum for a kicking strength of $V_0 \approx 1.35 \times 10^{-2}\mu$. It can be seen to revive, and eventually disperse over a wide range of wave-numbers. (b) Condensate densities at several times during the evolution. A pattern matching the optical potential can be observed to appear and disappear several times over the course of the evolution.	46
4.4	Condensate density at $t = 1.4 \times 10^{-2}$ s for several optical lattice rotation angles. The cell size of the super-lattice structures can be seen to shrink as the angle is increased. The angles for the examples shown are (a) $\theta_{\Delta} = 0$, (b) $\theta_{\Delta} = 2\pi/45$, (c) $\theta_{\Delta} = 4\pi/45$, (d) $\theta_{\Delta} = 2\pi/15$	47
4.5	Condensate density after receiving a kick with $\theta_{\Delta} = \pi/9$. The appearance and disappearance of a moiré structure with wavelength $\lambda_M \approx 2.9a$ over a timescale of about 50 ms can be seen.	47
4.6	Size of the resulting moiré super-structures as a function of the relative angle between the vortex and optical lattice. The dashed green line indicates the condensate radius. Inset: The different vectors in \mathbf{k} -space of the two lattices, with the optical lattice rotated by an angle θ_{Δ} . The $\mathbf{g}_W = \mathbf{g}_l - \mathbf{g}'_l $ vectors defining the dominant moiré wavelength are those for which the enclosed angle is smallest.	48
4.7	Compressible kinetic energy spectrum as a function of θ_{Δ} . All values are time-averaged over an interval $t = 0$ s to $t = 1$ s. The moiré peak corresponding to the lowest wave-number can be seen shifting to larger values for increasing angles and similar behavior is visible for the higher order components.	49

- 4.8 (a) For a kicking strength of $V_0 = 5.4 \times 10^{-2}\mu$ for a non-rotating condensate higher order modes become non-negligible contributions to the compressible kinetic energy spectrum. This leads to a variety of different density structures, with some close-ups shown for (b) 24 ms, (c) 36 ms, (d) 56 ms, and (e) 88 ms. Note that the larger structures in these plots are given by the optical lattice constant, which sets the scale. 49
- 5.1 (top) Doubly charged central vortex. Doubly charged vortex remains stable, and retains 6-fold symmetry of vortex lattice. (bottom) Doubly charged central vortex, and removal of nearby vortex. Doubly charged vortex remains stable, and forms 8-fold symmetry of vortex neighbours. 53

List of Tables

2.1	The approximate times taken to simulate the propagation of an atom through our atom chip system on both GPU and CPU.	35
-----	--	----

Introduction

This is the introduction. You might want to leave it unnumbered, as it is now. If you want to number it, treat it like any other chapter.

Chapter 1

Literature review

In this document I review the area of cold atomic gases, and in particular the superfluid behaviour of Bose–Einstein condensate systems. The history of this area will be discussed, highlighting both theoretical and experimental observations. With the fundamentals of Bose–Einstein condensation explained, I will then examine the dynamical behaviour of condensates from the perspective of superfluidity. Vortex behaviour will be discussed, along with recent results, concentrating on the dynamics of vortices in response to external potentials.

Following this, quantum chaos will be introduced, along with the many of the interesting dynamics that can be observed in superfluid flow. The creation and observation of quantum chaotic dynamics in a Bose–Einstein condensate shall be proposed. The goal of the proposed project will be to generate chaotic dynamics using a vortex lattice subjected to a periodically pulsed optical lattice. Beginning with a well defined state, generation of chaotic behaviour shall be examined. The Hamiltonian required to generate a vortex lattice in a condensate shall be mapped to the delta-kicked harmonic oscillator Hamiltonian, which will provide a model system to understand the observed system dynamics. To characterise the resulting dynamics, the trajectories of the vortices shall be plotted over the course of the evolution of the system. Further information may be obtained by examining the system using phase-space methods and Floquet theory to characterise the observed behaviours. Experiments to observe chaotic behaviour in the quantum regime are rare, and the realisation of this type of system should allow for the first of its kind to observe chaos in a system of well-ordered topological excitations. Given recent experimental progress in the area of trapping, cooling, rotating and controlling Bose–Einstein condensates, the proposed system should be realisable with currently available experimental techniques.

1.1 Cold atoms

1.1.1 Cooling of atomic gases

One of the major advances in experimental physics in recent times has been the laser cooling of trapped atoms to temperatures near absolute zero. This feat, which garnered the Nobel Prize in Physics in 1997, resulted from the pioneering work of C. Cohen-Tannoudji, S. Chu and W. Phillips [? ? ?]. It relies on the use of counter-propagating

detuned laser fields which are directed upon a trapped cloud of atoms. Due to Doppler shifting of the frequencies, atoms moving towards the respective beams see resonant photons, absorb them and slow down due to the momentum absorbed, with this technique being termed Doppler cooling. This is followed by a spontaneous emission in a random direction, for which the recoil kicks average out to zero. Hence, the atoms become cooler. As a result, the atoms will eventually reach a velocity below that which will cause an absorption from the lasers, leaving a less broad velocity distribution. Although laser cooling allowed temperatures to reach micro-Kelvin regimes, additional techniques must be used to obtain atoms deep in the nano-Kelvin temperature range. One such method, known as evaporative cooling, involves relaxation of the trapping potential height, which in turn allows many of the higher energy atoms to escape [?]. The remaining atoms rethermalise and are thus of lower energy, and therefore at a lower temperature. With these techniques the creation of Bose–Einstein condensates in dilute atomic gases became possible.

1.1.2 Introduction to Bose–Einstein condensation

Bose–Einstein condensation was theoretically predicted by N. Bose and A. Einstein [?]. This began as a work on the statistical behaviour of photons, eventually leading to the derivation of the “Bose–Einstein distribution” for an ideal bosonic gas. In the framework of the grand canonical ensemble and following the description given by Pitaevskii and Stringari [?, chap. 2], the Bose–Einstein distribution is given by

$$\bar{n}_i = \frac{1}{e^{\beta(\epsilon_i - \mu)} - 1}, \quad (1.1)$$

where \bar{n}_i is the average occupation number of the i -th energy state, $\beta = (k_B T)^{-1}$ with k_B being the Boltzmann constant and T as the temperature, ϵ_i is the i -th energy eigenvalue, and μ is the chemical potential giving the energy required to add an atom to the system. The total number of particles in the system, N , can be evaluated by summing over the individual occupation numbers, as

$$N = \sum_i \bar{n}_i. \quad (1.2)$$

This work predicted that non-interacting, indistinguishable (bosonic) particles would, if their energy was sufficiently low, undergo a phase transition below a critical temperature into a new phase in which the atoms would occupy the same lowest lying energy state of the system. The number of atoms occupying this lowest lying state, N_0 , is given by the relationship

$$N_0 \equiv \bar{n}_0 = \frac{1}{e^{\beta(\epsilon_0 - \mu)} - 1}, \quad (1.3)$$

with ϵ_0 representing the lowest energy eigenvalue. Since negative occupation numbers would be a nonphysical result, the chemical potential is limited to values of $\mu < \epsilon_0$. As μ tends to ϵ_0 the occupation of the lowest energy state grows large. Separating the total number of atoms into the lowest lying (condensed), N_0 , and higher lying (thermal), N_T , states as

$$N = N_0 + N_T = N_0 + \sum_{i \neq 0} \bar{n}_i(T, \mu), \quad (1.4)$$

a relation for the the onset of Bose–Einstein condensation can be given. This will happen when the temperature drops below a critical value, T_c , where μ will approach ϵ_0 , resulting in the macroscopic occupation of the lowest lying state, yielding a Bose–Einstein condensate (BEC).

BECs are a prime example of coherent matter waves, and demonstrate quantum mechanical effects on length-scales which can be considered mesoscopic. Given a cloud of identical bosons at higher temperature, the atoms exhibit billiard-ball type behaviour. As they are cooled, the thermal de Broglie wavelength of the atoms, given by

$$\lambda_{dB} = \sqrt{2\pi\hbar^2/mk_B T}, \quad (1.5)$$

where m is the atom mass, grows, causes the wave-nature of the atoms to become more prominent, and the atomic waves start to overlap when $\lambda_{dB} \approx$ inter-particle separation. The quantity $n\lambda_{dB}^3$, where n is the density of the gas, is known as the *phase-space density*. Physically this denotes the number of particles present in a box with sides of λ_{dB} length, and the phase transition to the condensate sets in at $\zeta(\frac{3}{2})$, where ζ is the Riemann-Zeta function [?]. The value of T_c for this to occur in a uniform gas is given by

$$k_B T_C = \frac{2\pi}{\zeta(\frac{3}{2})^{2/3}} \frac{\hbar^2 n^{2/3}}{m}, \quad (1.6)$$

or, in the case of a harmonic oscillator potential,

$$k_B T_C = \frac{\hbar\bar{\omega}N^{1/3}}{\zeta(3)^{1/3}}, \quad (1.7)$$

where $\bar{\omega} = (\omega_x\omega_y\omega_z)^{1/3}$ is the geometric mean of the oscillator frequencies. Critical temperatures for harmonically trapped gases are on the order of nano-Kelvin assuming realisable trapping frequencies, which were experimentally inaccessible during the time of Bose and Einstein.

Fritz London, in 1938, following on from the body of work derived by Einstein and Bose drew the connection between superfluidity in liquid ^4He and Bose–Einstein condensation [? , Chap. 1]. However, due to the liquid nature of ^4He at low temperatures only approximately 10% of the atoms condense into a BEC [?]. In order to achieve the large occupation of the lowest energy state the system must be prepared so that the interparticle interaction strength does not destroy the coherence, as is the case for liquid ^4He .

Due to their weak interactions, dilute atomic gases are closer to the ideal case discussed by Bose and Einstein. One negative impact, though, were the higher masses of the atoms used in such systems, which required reaching much lower transition temperatures. As such, the use of lighter elements were considered. Spin-polarised hydrogen was one of the first systems to be investigated to create BEC [? ?] in the 1970’s. Using trapping and cooling techniques present at the time, this type of system came close, but did not quite reach the required temperatures and phase-space densities for Bose–Einstein condensation to occur until over twenty years later [?]. Given the advent of laser cooling in the 1980’s, the use of alkali atoms was considered partly due to the ease of accessibility of their optical transition frequencies. It was not until 1995 that the first BECs would be experimentally realised [? ?].

1.1.3 Theoretical description of BECs: Gross–Pitaevskii equation

I will, in the following section, outline the derivation of the mean-field Gross–Pitaevskii equation, which is widely used to study the behaviour of the condensate in many works cited in this review. Following the *Les Houches 2013 Lecture Course* by J. Walraven [?] the second quantization form of the many-body Hamiltonian for interacting particles in a harmonic potential is given by

$$\hat{\mathcal{H}} = \hat{H}_1 + \hat{H}_2 = \int \hat{\Psi}^\dagger H_0(\mathbf{r}, \mathbf{p}) \hat{\Psi} d\mathbf{r} + \frac{1}{2} \int \hat{\Psi}^\dagger \hat{\Psi}^\dagger V_{\text{int}}(\mathbf{r}' - \mathbf{r}) \hat{\Psi} \hat{\Psi} d\mathbf{r}' d\mathbf{r}, \quad (1.8)$$

with $H_0(\mathbf{r}, \mathbf{p}) = -\frac{\hbar}{2m} \nabla^2 + V_{\text{ext}}(\mathbf{r})$. The external potential, $V_{\text{ext}}(r)$ is taken as harmonic, of the form

$$V_{\text{ext}}(\mathbf{r}) = \frac{m}{2} \sum_i \omega_i r_i^2, \quad (1.9)$$

and with ω_i representing the trapping frequency in the i -th spatial dimension. The interaction potential, V_{int} is assumed to be point-like as

$$V_{\text{int}}(\mathbf{r}_i, \mathbf{r}_j) = g \delta(\mathbf{r}_i - \mathbf{r}_j), \quad (1.10)$$

where δ is the Dirac delta function and the mean-field interaction, g is given by

$$g = \frac{4\pi\hbar^2 a_s}{m}, \quad (1.11)$$

with a_s being the s-wave scattering length. Inserting the contact potential Eq. (1.10) into the second quantised interaction Hamiltonian \hat{H}_2 from Eq. (1.8) above yields the following relations

$$\hat{H}_2 = \frac{g}{2} \int \hat{\Psi}^\dagger(\mathbf{r}) \hat{\Psi}^\dagger(\mathbf{r}') \delta(\mathbf{r} - \mathbf{r}') \hat{\Psi}(\mathbf{r}') \hat{\Psi}(\mathbf{r}) d\mathbf{r} d\mathbf{r}' \quad (1.12)$$

$$= \frac{g}{2} \int \hat{\Psi}^\dagger(\mathbf{r}) \hat{\Psi}^\dagger(\mathbf{r}) \hat{\Psi}(\mathbf{r}) \hat{\Psi}(\mathbf{r}) d\mathbf{r} \quad (1.13)$$

$$= \frac{g}{2} \int \hat{\Psi}^\dagger(\mathbf{r}) \hat{n}(\mathbf{r}) \hat{\Psi}(\mathbf{r}) d\mathbf{r}. \quad (1.14)$$

In the Heisenberg picture, the evolution of the system is governed by the equation

$$i\hbar \frac{\partial}{\partial t} \hat{\Psi}_H(\mathbf{r}, t) = [\hat{\Psi}_H(\mathbf{r}, t), \hat{\mathcal{H}}], \quad (1.15)$$

where the Heisenberg field annihilation operator, $\hat{\Psi}_H(\mathbf{r}, t)$, is given by

$$\hat{\Psi}_H(\mathbf{r}, t) = e^{\frac{i\hat{\mathcal{H}}t}{\hbar}} \hat{\Psi}(\mathbf{r}) e^{-\frac{i\hat{\mathcal{H}}t}{\hbar}}. \quad (1.16)$$

The operator, $\hat{\Psi}_H$ can be interpreted as the one removing an atom from a given state of the system. Therefore, if all N atoms in the system are in the ground-state, $|0_N\rangle$,

as would be the case in an ideal condensate, the following relationship holds

$$\hat{\Psi}_H(\mathbf{r}, t)|0_N\rangle = e^{\frac{iE_0(N-1)t}{\hbar}}\hat{\Psi}(\mathbf{r})e^{\frac{-iE_0(N)t}{\hbar}}|0_N\rangle \quad (1.17)$$

$$= \hat{\Psi}(\mathbf{r})e^{\frac{i[E_0(N-1)-E_0(N)]t}{\hbar}}|0_N\rangle \quad (1.18)$$

$$= \hat{\Psi}(\mathbf{r})e^{\frac{-i\mu t}{\hbar}}|0_N\rangle, \quad (1.19)$$

where $\mu = E_0(N) - E_0(N-1)$ is the chemical potential. Using the bosonic commutation relations

$$\left[\hat{\Psi}(\mathbf{r}'), \hat{\Psi}^\dagger(\mathbf{r})\right] = \delta(\mathbf{r}' - \mathbf{r}), \quad (1.20)$$

$$\left[\hat{\Psi}(\mathbf{r}'), \hat{\Psi}(\mathbf{r})\right] = \left[\hat{\Psi}^\dagger(\mathbf{r}'), \hat{\Psi}^\dagger(\mathbf{r})\right] = 0, \quad (1.21)$$

and noting the following relations

$$\left[\hat{\Psi}(\mathbf{r}), \hat{H}_1\right] = \hat{H}_0(\mathbf{r}, \mathbf{p})\hat{\Psi}(\mathbf{r}), \quad (1.22)$$

$$\left[\hat{\Psi}(\mathbf{r}), \hat{H}_2\right] = g\hat{n}(\mathbf{r})\hat{\Psi}(\mathbf{r}), \quad (1.23)$$

$$\left[\hat{\Psi}(\mathbf{r}), \hat{n}\right] = \hat{\Psi}(\mathbf{r}), \quad (1.24)$$

the Hamiltonian Eq. (1.8) can be rewritten in the following form

$$\mathcal{H} = \sum_{i=1}^N \left(-\frac{\hbar^2}{2m} \nabla^2 + V(\mathbf{r}_i) \right) + \frac{1}{2}g \sum_{i \neq j} \delta(\mathbf{r}_i - \mathbf{r}_j). \quad (1.25)$$

Due to the macroscopic occupation of the lowest lying single-particle state, $\hat{\Psi}$ can be treated as a classical field, Ψ , neglecting all quantum fluctuations involving higher-lying states. Substituting Eq. (1.25) and (1.16) into (1.15), the time dependent mean-field Gross-Pitaevskii equation (GPE) can then be written as

$$i\hbar \frac{\partial}{\partial t} \Psi(\mathbf{r}, t) = \left[-\frac{\hbar^2}{2m} \nabla^2 + V(\mathbf{r}) + g|\Psi(\mathbf{r}, t)|^2 \right] \Psi(\mathbf{r}, t). \quad (1.26)$$

The time independent form can be found by substituting Eq. (1.19) into (4.2), yielding

$$\mu \Psi(\mathbf{r}) = \left[-\frac{\hbar^2}{2m} \nabla^2 + V(\mathbf{r}) + g|\Psi(\mathbf{r}, t)|^2 \right] \Psi(\mathbf{r}), \quad (1.27)$$

where the wavefunction is normalised to the particle number, N , as follows

$$\int_{-\infty}^{\infty} d\mathbf{r} |\Psi(\mathbf{r})|^2 = N. \quad (1.28)$$

In the case of a rotating condensate an additional term appears in the GPE, $-\Omega L$, where Ω is the angular rotation frequency, and L is the angular momentum. Assuming

rotation about a single axis, the longitudinal direction, z , L can be replaced with L_z , giving the final form of the GPE in the co-rotating frame as

$$i\hbar \frac{\partial}{\partial t} \Psi(\mathbf{r}, t) = \left[-\frac{\hbar^2}{2m} \nabla^2 + V(\mathbf{r}) + g|\Psi(\mathbf{r}, t)|^2 - \Omega L_z \right] \Psi(\mathbf{r}, t). \quad (1.29)$$

This mean-field equation can be used to describe the behaviour of the condensate, provided the number of atoms is sufficiently large ($> 10^3$ for most experimental set-ups) and the correlations are not too strong. Assuming a large number of bosons in the condensate, N , the interaction term dominates over the kinetic term of the Hamiltonian which can therefore be neglected. This turns finding the ground-state of the system into a solvable, algebraic problem, and is known as the Thomas-Fermi approximation [? , p. 84]. The Hamiltonian can thus be reduced to a combination of the trapping potential and the mean-field interaction, and the wavefunction, ψ_{TF} , can be determined from the time independent GPE as

$$\psi_{TF}(\mathbf{r}) = \sqrt{g^{-1}[\mu - V(\mathbf{r})]\Theta(\mu - V(\mathbf{r}))}, \quad (1.30)$$

where μ is the chemical potential, and Θ is the Heaviside step function, which ensures that the condensate density does not become negative. Within this regime the condensate can be described by hydrodynamical equations [? , Pg. 180], and from this, an approximate value for the cloud radius can be determined, called the Thomas-Fermi radius. The boundary of the cloud is determined by the surface at which the density becomes zero, and corresponds to the point where the trapping potential and chemical potential are equivalent. This gives the geometric mean spatial extent of the cloud [? , p. 169] as

$$\bar{R} = \left(\frac{15Na}{\bar{a}} \right)^{1/5} \bar{a}, \quad (1.31)$$

where the characteristic length of the harmonic oscillator is given by $\bar{a} = \sqrt{\hbar/m\bar{\omega}}$. Thus, within the Thomas-Fermi radius, it is possible to explain the behaviour of the BEC analytically and compare with exact numerical results from integrating the full GPE.

1.1.4 Realisation of Bose–Einstein condensation in dilute gases

Following the first experimental realisations of a BEC in dilute atomic gases by E. Cornell and C. Wiemann at University of Colorado, Boulder [?], and W. Ketterle at M.I.T. [?], work was carried out by Baym and Pethick [?], who investigated the mean-field ground-state solution in the Thomas-Fermi limit of a magnetically trapped rubidium BEC, as was created in the Boulder experiment.

In a first comprehensive review of the area only a few years later by Dalfovo *et al.* [?], the underlying theory of trapped Bose–Einstein condensates was examined in detail. The review discusses how the combination of laser cooling and evaporative cooling [?] allowed the experimentalists to reach the temperatures and required phase-space densities for Bose–Einstein condensation to occur. Ground-state properties of the system are examined assuming an effective interaction. Stationary properties of

harmonically trapped condensates are discussed, in the framework of mean-field theory (Gross–Pitaevskii), which is shown to allow for the determination of system properties and dynamics. Attractive versus repulsive interactions are examined, followed by a discussion of “Beyond mean-field theory”, where corrections to the theory are applied to enable more exact determination of ground-state energies.

The nature of vortices in a condensate are considered, and in particular critical angular velocities, core size, and imaging. Given the coherence of atoms in a condensate, matter-wave interference by simply expanding and overlapping two condensates is suggested, and the appearance of a dislocation in the interference pattern is a sign of the presence of a vortex. The authors further indicate the accurate agreement of mean-field theory with known experimental data, and differences between observation and mean-field predictions are mentioned.

Interpenetrating condensates are discussed in a paper by Sinatra *et al.* [?], where the authors present a theoretical prediction of the mixing of a two-component, initially separated condensate. Predicted oscillations of the mean condensate separation were compared to the Boulder (JILA) experiment, and showed good agreement, supporting the use of mean-field theory in predicting condensate dynamics.

1.1.5 Lower dimensional condensates

Another area of interest in BEC systems is that of low-dimensional condensates, such as the work undertaken by Görlitz *et al.* [?], wherein a strong axial confinement of the condensate in the z -dimension is used to effectively create a “pancake” condensate in an optical trap. This trapping geometry restricts motion in the axial direction, creating effective two-dimensional dynamics. This may be extended further to one-dimension by using elongated “cigar” traps via magnetic potentials, such as those existing on atom-chip structures [? ? ?], or in optical potentials. Görlitz *et al.* state that in lower dimensional systems phenomena such as solitons and vortices should have much greater stability, and should therefore be more suitable for investigating them. Realisation of a Tonks–Girardeau gas is also discussed, with such systems becoming accessible using optical potentials such as described by Moritz *et al.* [?]. Work in the effective 2D regime is of particular interest, and condensate behaviour in relation to excitations has been examined under such conditions. Kimura [?] investigates the dynamical behaviour of condensate breathing modes in both two and one dimensions. Tanatar *et al.* [?] consider the use of a tightly-confined pancake condensate, and discuss differences occurring to the inter-atomic scattering as a function of confinement strength along the z -dimension. Both mentioned works consider use of the Thomas–Fermi approximation, comparing results obtained analytically with that of numerical integration using the Gross–Pitaevskii equation.

1.2 Superfluidity

1.2.1 Introduction to superfluidity

A classical fluid in a rotating vessel will eventually reach a steady-state wherein the fluid rotates as a whole with the container as a solid-body. This behaviour emerges as a result of the viscosity of the fluid and, assuming the no-slip condition [?], that the fluid elements in direct contact with the boundary of the container adhere to its surface. Given sufficient time to reach equilibrium, the entire fluid will rotate at the same angular velocity. If the driving forces are removed, this flow will eventually cease to rotate, and once again become stationary. Such flow can be contrasted with that of an inviscid flow, and will not experience any effect from the boundary rotation. Once in motion, an inviscid fluid will continue to rotate indefinitely. This type of flow can be realised with superfluids [?].

Superfluidity is a macroscopic quantum effect that is closely related to Bose–Einstein condensation. Liquid helium has been known for many years to exhibit this superfluid behaviour [?]. One interesting property of superfluids is that they have quantized circulation which can lead to the appearance of quantum vortices under rotation. Traditionally, such excitations have been created in liquid ^4He by a “rotating bucket” type of experiment, where the container is rotated about a single axis. When the fluid is initially above the λ -critical point, the temperature at which ^4He moves from a classical fluid to a superfluid, the atoms will undergo solid-body rotation with the container. On cooling the atoms below the λ -critical point liquid ^4He will undergo a transition to the superfluid state. If the velocity is above a critical rotation value vortices are nucleated in the rotating superfluid helium system. Due to the strongly interacting nature of liquid helium the nucleated vortices are difficult to visualise as the healing length, ξ , of liquid ^4He , the length over which the central zero density core of a vortex increases to the superfluid bulk density, is on the order of Ångströms [?].

In order to visualise such vortices experimentally it was necessary to use an indirect means of visualisation in the form of tracer particles [?]. Limited success was had with this technique using solid hydrogen, and later plastic microspheres, as they tended to join together due to static charges. An improved technique, using charged particles, showed much greater success [?]. Ions, or electrons, were trapped inside the vortex lines, and an electric field along the direction of the lines allowed for acceleration of the charges towards a luminescent screen where they could be observed. Current experimental work in vortex visualisation with liquid ^4He has advanced significantly [? ?], yet fine control over the behaviour of the liquid and the vortex dynamics remains difficult.

Superfluid behaviour is observed in liquid helium due partly to a portion of the atoms condensing into the ground-state. Given that BECs show superfluidity, the use of a dilute gas where the majority of atoms are in the condensate state provides a more controlled means to investigate superfluidity and quantised vortices [? ? ? ?]. In contrast with liquid ^4He , having a healing length of the order of nanometers, the healing length of a dilute gas of alkali atoms is on the order of microns [?]. This places condensates in a much more accessible regime for visualising vortices compared with liquid ^4He experiments. To fully understand the behaviour of the system, it is necessary

to have a framework for modelling the condensate, in the absence and the presence of vortices. A dilute gas of condensed atoms close to absolute zero temperature can be readily modelled by the Gross–Pitaevskii equation (1.29), offering a direct means to simulate condensate behaviour. It is useful to obtain a hydrodynamic description for the condensate, performed by treating its wave-function as

$$\Psi(\mathbf{r}, t) = |\Psi(\mathbf{r}, t)|e^{i\theta(\mathbf{r}, t)}, \quad (1.32)$$

where $\theta(\mathbf{r}, t)$ is the condensate phase, and $|\Psi(\mathbf{r}, t)| = \sqrt{\rho(\mathbf{r}, t)}$, the square root of the condensate density [?, chap. 1]. The formalism used below follows that given by Ueda [?], where the condensate density is given by

$$\rho(\mathbf{r}, t) = \Psi^*(\mathbf{r}, t)\Psi(\mathbf{r}, t) = |\Psi(\mathbf{r}, t)|^2. \quad (1.33)$$

The continuity relation takes the form

$$\frac{\partial}{\partial t}\rho(\mathbf{r}, t) + \nabla \cdot \mathbf{j}(\mathbf{r}, t) = 0, \quad (1.34)$$

where the current density of the condensate is

$$\mathbf{j}(\mathbf{r}, t) = \frac{-i\hbar}{2m} [\Psi^*(\mathbf{r}, t)\nabla\Psi(\mathbf{r}, t) - \Psi(\mathbf{r}, t)\nabla\Psi^*(\mathbf{r}, t)]. \quad (1.35)$$

Using ansatz (1.32) and substituting it into Eq. (1.35) then gives the form for the current density,

$$\mathbf{j}(\mathbf{r}, t) = |\Psi(\mathbf{r}, t)|^2 \frac{\hbar}{m} \nabla\theta(\mathbf{r}, t). \quad (1.36)$$

The velocity of the superfluid, $\mathbf{v}(\mathbf{r}, t)$ is defined as the ratio of the current density to the density, and then is given by

$$\mathbf{v}(\mathbf{r}, t) \equiv \frac{\mathbf{j}(\mathbf{r}, t)}{\rho(\mathbf{r}, t)} = \frac{\hbar}{m} \nabla\theta(\mathbf{r}, t). \quad (1.37)$$

The gradient of the phase therefore gives the velocity of the condensate atoms; this indicates that the superfluid behaviour in a condensate is irrotational ($\nabla \times (\nabla\theta) = 0$). Assuming a closed loop integral about a central point in the condensate, and recalling the single-valued nature of the wavefunction, yields the relationship

$$\oint_C \mathbf{v} \cdot d\mathbf{l} = \frac{\hbar}{m} 2\pi l. \quad (1.38)$$

This shows the quantised nature of circulation in a superfluid, with l representing the integer charge of the circulation. The phase winding around the central region is given by multiples of 2π , with the centre of the phase becoming ill-defined. To circumvent this problem the density at this point drops to zero, signalling the presence of a vortex in the condensate density. This drop happens over the scale of the healing length, which, for repulsive interactions, is given by

$$\xi = \frac{1}{\sqrt{8\pi\rho a_s}}, \quad (1.39)$$

where ρ is the bulk density of the condensate, and a_s is the s-wave scattering length. To sustain a vortex the condensate must have sufficient angular momentum, which is imparted via the angular momentum term $-\Omega L_z$ in the Hamiltonian given by Eq. (1.29). This term accounts for rotation of the condensate, and puts us in the co-rotating frame. The angular velocity, Ω , of the condensate has an upper-bound stability limit equivalent to the transverse trapping frequency, ω_\perp , of the harmonically trapped condensate.

I will now further discuss both theory and experimental results for vortex behaviour in condensate systems.

1.2.2 Vortices in Bose–Einstein condensates

In [?] Stringari derives equations for the moment of inertia for the condensate, and shows that above T_c the moment of inertia can be described classically. Below T_c the moment of inertia is represented as a sum of two terms, one describing the classical solid-body rotation of the thermal cloud, the other describing the irrotational flow of the condensed cloud. At zero Kelvin, the moment of inertia is given entirely by the irrotational component, indicating that all atoms are condensed.

A paper by Dalfovo and Stringari [?] suggested the possibility of exciting vortices using an anisotropy in the trapping potential. The authors discuss the applicability of mean-field Gross–Pitaevskii theory to a such problem. An examination into the behaviour of vortex flow is given and the solutions for the ground-state and vortex carrying states are found via numerical minimisation of the Gross–Pitaevskii energy functional. A decrease in the critical angular velocity for vortex formation with an increase in the number of condensate atoms, N , is shown. For attractive interactions, the critical angular velocity increases with larger N . Ground-state results are compared to experimental data from the JILA (Boulder) experiment [?], and were found to be in good agreement. A closely related work is one by Barenghi [?], who discusses finite temperature corrections to the zero temperature regime to account for displacements of the vortex cores. It shows how small thermal excitations can, even at low temperatures, affect the vortex position. The work of Lundh *et al.* [?] further extends that of Dalfovo and Stringari. Here, the authors investigate the lowest required angular velocity that allows a vortex to enter a condensate, and consider corrections to the Thomas–Fermi approximation. They discuss the use of both isotropic and anisotropic trapping geometries, and find good agreement between the numerical integration of the GPE for experimentally realistic parameters, and analytical expressions they derive for the kinetic energy and the lower-bound on the critical angular velocity for a vortex to enter the atomic cloud.

Marzlin *et al.* [?] proposed a different method for generating vortex states. They consider a condensate subjected to two Laguerre–Gaussian beams of σ^+ and σ^- polarisation respectively. The beams are chosen to be resonant with an internal transition, and transfer angular momentum through the coupling allowing the condensate to start rotating. Another method, investigated numerically by Jackson *et al.* [?] uses a blue-detuned light field to simulate an object moving through an effective two-dimensional BEC, which can be achieved by tightly confining it in the z -direction. They show the formation of vortices close to the centre of the laser potential, whose movement causes

a “phase-slip”, with the value of the phase going from $-\pi$ to π around the vortex. They also note that the speed of vortex shedding from the object has an inverse relationship to the speed of sound in the condensate, given as

$$c(\mathbf{r}, t) = \sqrt{\frac{\rho(\mathbf{r}, t)U}{m}}, \quad (1.40)$$

where $U = 4\pi\hbar^2 a_s/m$ represents the repulsive atom-atom interaction [?]. A second paper by Marzlin *et al.* [?] suggests the use of an optical dipole potential resulting from four travelling-wave beams to excite a trapped condensate and induce circulation by transfer of angular momentum. Results of this study show that for harmonic trapping potentials a superposition of vortex states is created. Pure vortex states are shown to arise only from anharmonic traps combined with a rotating linear potential. This topic is treated by the same authors in a follow up work [?].

Building upon the earlier discussion by Marzlin *et al.*, Goldstein *et al.* [?] consider schemes for accurate detection of the topological charge of a trapped condensate containing vortices. Their idea builds on the interference of the vortex carrying condensate with a second ground-state condensate, and they show that the vanishing of interference lines is related to the vortex charge. A work provided by Svidzinsky *et al.* [?] discusses the hydrodynamic formalism within the Thomas-Fermi limit, and show it is an effective means of describing condensate behaviour in the presence of vortices. An alternative approach is presented by Lundh *et al.* [?], who consider methods for vortex detection methods in large condensates. They discuss the difficulties that arise when only a single vortex is present, as the energy difference to the vortex-less ground state would be too small to measure. They consider the free expansion of both a two and three-dimensional condensate, which allows a singly charged vortex core to expand as well and become visible on an absorption picture. They note that in two-dimensions (2D) the vortex core and condensate expand at roughly the same rate, making detection somewhat more challenging than in three-dimensions (3D) where the core initially expands faster than the condensate. Lundh *et al.* also note that in the limit of weak coupling a difference exists between the aspect ratios of condensates with and without vortices, and that this effect is enhanced by anisotropic trapping geometries.

The stability of vortex states in a condensate is also a widely discussed topic [? ?], as non-rotating traps show an instability for small displacements of the vortex from the trap centre. However, Feder *et al.* [?] calculated the critical rotation frequencies for vortex stabilisation at the centre of an anharmonic rotating trap. Further proposed schemes to realise vortex carrying condensates are given by the following theoretical works [? ? ? ?]. The method proposed by Dobrek *et al.* [?], shows a means to optically generate vortices by the use of what they term a “phase-imprinting” method. The authors describe a scheme where the phase of the condensate is controlled directly, and given the required topological charge to induce a vortex during evolution. Through use of an absorption plate whose axis angle depends on the absorption coefficient, the condensate can be imprinted with the required phase pattern.

The realisation of vortices in a two-component condensate was first achieved by Matthews *et al.* [?]. Using two internal states of ^{87}Rb , the authors coherently coupled and induced transitions between both in such a way that one component acquired a 2π phase winding and rotated around the other component. A different route to creating

vortices was successfully used by Madison *et al.* [?], who tightly focused a laser to stir the condensate beyond a critical frequency for nucleation. This way they were able to generate multiple vortices in the condensate.

1.2.3 Vortex lattices

In early 1999, Castin and Dum [?] examined the ground-state solutions for multi-vortex condensates, simulating up to 18 vortices. Their work is mostly performed in effective 2D, with data for a 3D configuration given following the main body of work. At the same time Feder *et al.* [?] considered the case where multiple vortices are present in the condensate, and performed a numerical investigation of this on a 3D condensate of ^{23}Na . The authors further mention that given a sufficient number of vortices in the condensate an almost regular triangular array would be observed. Evidence for this behaviour could be seen in the experimental data obtained by Madison *et al.* [?], showing up to 11 vortices that seemingly arrange in a triangular array pattern. This resulted from laser stirring of the condensate, and was also covered in [?]. A follow-up study by Madison *et al.* [?], and Chevy *et al.* [?] showed the relationship between vortex nucleation and the dynamical instabilities arising from the irrotational state, specifically, the excitation of the rotating quadrupolar mode of the condensate.

Of all the work on multiple vortex generation and the underlying theory, one of the seminal works of the time was the experiment from Ketterle's group on vortex lattices [?]. The authors begin with a comparison of vortices to the type of behaviour observed in type-II superconductors, where penetration of the magnetic field into the conductor is possible only via quantised flux lines. They then state that “(v)orticity can enter rotating superfluids only in the form of discrete line defects with quantized circulation”, and therefore establish a close connection between the rotational properties of superfluids and superconductors. Furthermore, their experiment finds Abrikosov (triangular) style vortex lattices, which are also known from type-II superconductors. The group generated condensates with lattices containing upwards of 130 vortices, in a well ordered triangular formation. This was achieved through stirring of the condensate with a blue-detuned laser which was moved symmetrically around the condensate at a specified angular frequency, Ω . The conclusions drawn by the authors are that BECs are a robust system for generating vortex lattice structures that naturally form into a regular triangular pattern, and show many similarities to type-II superconductors.

Ho [?] showed that the behaviour observed in the fast rotation limit closely resembles that of the two-dimensional quantum Hall regime, where the system is residing in the lowest Landau level, *LLL* ($n = 0$). Ho states that the experimental data suggests the MIT group has not yet reached the *LLL* regime, but are very close. As the rotation of the cloud approaches the trapping frequency, the system tends to the *LLL*. However, in this regime the Thomas-Fermi approximation becomes invalid, requiring a more accurate consideration of the z -components. He concludes by stating that rotation close to the trap frequency will require treatment beyond that of the mean-field approach. An additional study from the MIT group [?] derived a result showing that the number of vortices in the condensate is proportional to the rotational frequency of the stirrer at a given frequency. They discuss the cause of vortex nucleation as a consequence of surface modes in the condensate and due to localised regions of turbulent behaviour.

The group at JILA devised a method to systematically evaporatively cool and rotate a cloud of ^{87}Rb confined in a harmonic potential [?]. Beginning with a normal fluid component close to T_c , the harmonic trapping potential is initially deformed and rotated. This induces a rotation of the cloud, until it enters a solid-body rotational state with the trap. Upon reaching a steady-state, the rotating asymmetry is switched off, and the cloud is evaporatively cooled. This approach is similar to that of the rotating bucket experiment in liquid ^4He . By applying an additional distortion to the trapping geometry allows for the removal of atoms with large axial displacements to take place, and as a result of this, the temperature of the cloud is reduced by a factor of four. Additionally, the rotation rate of the remaining cloud increases as the angular momentum per particle stays close to constant. At the end of the evaporation process, a condensate forms at the centre of the cloud, rotating with a frequency as high as 0.94 times the confining potential frequency. Results are compared with the theoretical calculations of Feder and Clark [?], and were stated to agree.

Although a large number of works exist which investigate systems with low numbers of vortices [? ? ? ? ?], I will concentrate primarily on studies of systems containing a large number of vortices. Engels *et al.* [?] were capable of creating condensates containing equivalent numbers of vortices to those obtained in the MIT experiments, and investigated the behaviour of these lattices with respect to excitation of higher lying modes. The authors show a “sheetlike structure” of the condensate vortices in the presence of an $m_z = -2$ surface mode. It is discussed that due to the difficulty in obtaining dense vortex lattices in pancake-like condensates that this may provide a means to investigate such behaviour.

Adhikari *et al.* [?] carried out numerical simulations of condensate behaviour subjected to a sudden perturbation of the trapping potential. The authors discuss changes in the interaction strength, the trapping potential, and the rotation of the condensate, and how a vortex will decay once rotation has ceased. Their simulations considered quasi (effective) two-dimensional condensates and solved the GPE using a split-operator technique [?]. Subjected to a perturbation pulse the condensate boundary starts to oscillate, and the number of supported vortices changes dependent upon the sign of interaction change or trapping potential.

1.2.4 Fast rotation limit

Mueller and Ho [?] considered the case of a two-component condensate under fast-rotation, above the previously reported rotation rates that were experimentally accessible. Such systems are stated to be in the “mean-field quantum Hall regime”, where each component can be described by an individual wave-function with an angular momentum large enough to ensure the LLL regime. These systems are a generalisation of the work by Ho [?], and the authors show that the minimum energy state corresponds to a pair of interspersed vortex lattices, one for each respective component. They also show that variation of the interaction parameters allows the geometric arrangement of the lattices to be modified, for example into a rhombic structure. An additional theoretical examination of vortices in the quantum Hall regime ($\Omega \approx \omega_\perp$) is offered by Subrahmanyam [?]. At such rotation rates the aspect ratio of the condensate, namely the ratio of the width in the z -dimension to the width in the x - y plane, becomes very

small yielding an effective two-dimensional system. It is also stated that in this limit the use of mean-field theory will fail due to perturbations becoming more prominent, and a full model for interacting bosons becomes necessary to fully describe the dynamics. For rotation rates less than this limit, however, the vortices arrange themselves into the expected triangular lattice. This work in the mean-field quantum Hall (MFQH) regime is further extended by Regnault and Jolicoer [?], who describe fractional quantum Hall (FQH) behaviour in condensate systems by using a non mean-field formalism. For the body of work I describe later, it will be assumed that the rotation rates will remain below FQH regime rotation rates, allowing for a MFQH description.

Given the known upper limit of the rotational frequency for which a harmonically trapped condensate is stable, which is the harmonic trapping frequency, one might inquire as to whether other configurations exist in which higher rotation rates can be achieved. An investigation performed by Bretin *et al.* [?] considers a condensate trapped within a quadratic plus quartic (QQ) potential, with an additional theoretical analysis for both the repulsive and attractive interaction cases given by Ghosh [?]. Bretin *et al.* examine the behaviour of the system at the limiting point $\Omega = \omega_{\perp}$, stating that the angular momentum of the system becomes singular. A comparison is made to a charged particle in a magnetic field, with an energy spectrum reminiscent of Landau levels with a $2\hbar\omega$ separation, as stated previously by Mueller and Ho [?]. Through inclusion of the additional quartic term, the system can be examined at rotation frequencies at, and slightly beyond, the trapping frequency. Rotation frequencies of up to $0.95\omega_{\perp}$ are shown to result in regular vortex lattices, with values beyond this inducing distortions to the structure of the lattice. The authors also mention that at rotation frequencies close to the trapping frequencies significant time is required “to reach a well ordered vortex lattice” when performing imaginary time evolution to find the system ground-state. The observation of giant vortices, which are possible within this regime, are mentioned but not discussed in much detail.

The creation of such a MFQH system which can be described by the LLL was another milestone for the JILA group, and was reported in a paper by Schweikhard *et al.* [?]. The authors successfully demonstrate a condensate rotated upwards of 0.99 times ω_{\perp} . Given that this regime displays behaviour different to the known results at the time, the importance of comparing the regime to the well known Thomas–Fermi limit was an important next step. Such a work was carried out by Watanabe *et al.* [?]. They showed that the density profile of the rotating condensate in the MFQH limit was described well by the Thomas–Fermi approximation. This was shown to hold true provided that the number of vortices is much larger than unity, or that the condensate size is large in comparison with the harmonic oscillator length in the transverse direction, $\bar{a}_{\perp} = \sqrt{\hbar/m\omega_{\perp}}$. Comparing the MFQH regime to the Thomas–Fermi limit was also studied by Zhai *et al.* [?] who investigated the behaviour of two overlapping vortex lattices.

As mentioned earlier, the Thomas–Fermi limit describes the case where the kinetic energy term of the Hamiltonian may be neglected in comparison to the interaction energy, as it offers little contribution to the condensate behaviour. This remains true for low rotation rates, however kinetic energy becomes important in the limit of fast rotation. In this case $\Omega/\omega_{\perp} \approx 1$, and the centrifugal force term, $m\Omega^2 r$, almost balances with the trapping force term, $-m\omega^2 r$. The kinetic energy term can no longer be

neglected here, but one may now consider the condensate in the MFQH regime. The interaction energy is then much less than the gap between energy levels for single particle Landau levels [?]. Zhai *et al.* state that the difference between these two regimes are characterised purely by the ratio of the kinetic energy to the interaction energy of the system, and in the MFQH regime we can thus assume the LLL has been achieved.

Assuming the LLL description for a fast rotating Bose–Einstein condensate, the Dalibard group provide many theoretical works using this framework, beginning with the work offered by Aftalion *et al.* [?]. The authors describe the case where the number of atoms to the number vortices, denoted as the “filling factor”, $\nu = N/N_v$ [?], becomes an important characteristic of the system. In the case where the number of vortices is small compared to the number of atoms (still under the fast rotation limit), the system may be accurately described to be in the MFQH regime. However, as the rotational frequency of the condensate approaches the trapping frequency, the condensate width expands, and will tend to infinity. In this limit the number of vortices is comparable to the number of condensate atoms, and the system can no longer be described by a single macroscopic wave-function. Instead it can be described as being similar to “an electron gas in the fractional quantum Hall regime”. To avoid dealing with the FQH regime, the authors restrict themselves to the MFQH regime, and choose rotational frequencies that guarantee this. The MFQH regime is entered when $1000 > \nu > 10$, which is attained close to the $\Omega/\omega_\perp \approx 1$ limit. One of the key conclusions from this paper is that the density distribution of the condensate in the MFQH regime is that of an inverted parabola, with the vortices forming a triangular lattice pattern that is almost regular. The area of each vortex cell differs from that of the solid-body rotating case, and is significantly distorted at the edge of the condensate. The results of Schweikhard *et al.* [?] are found to agree with what is proposed in this work, but they differ from the findings by Ho [?], which predicted a Gaussian density distribution with an infinite regular lattice. For an almost perfectly regular lattice, the rotation rate must be sufficiently large that the condensate width extends to large distances and a large number of vortices are generated, without entering the FQH regime. For such a system, the vortices about the central region will be uniformly ordered due to the balanced velocity fields. Vortices on the condensate edge will have a distorted alignment, and can be neglected.

A closely related work undertaken by Stock *et al.* [?] offers a brief review of many of the results relevant to vortex behaviour in condensates, up to and beyond the $\Omega = \omega_\perp$ regime. They discuss many of the known results in the MFQH regime, analogies to Landau levels, the use of QQ potentials, and briefly the FQH regime. Vibrational modes of vortex lattices, such as the Kelvin and Tkachenko modes, which are oscillations of the vortex line and vortex lattice respectively, are also reviewed. The use of QQ potentials is discussed as a way to allow observation of vortices with winding numbers larger than unity, where a purely quadratic potential would be unstable. Finally, they restate the fact that when the number of vortices approaches the atom number of the condensate, the system will no longer be capably described by a mean-field theory. Instead it enters a strongly correlated regime mirroring that of FQH regime, the observation of which is experimentally possible only for low atom numbers. A similarly comprehensive review of experimental results is offered by Srinivasan [?], and covers much of the same

material, albeit with greater detail in parts.

Given the wealth of literature available on rotating condensates, a review of all experimental and theoretical results then available was compiled and published by Fetter [?]. The author draws some conclusions and defines a future outlook for the field.

- Theory and experiment agree well for rotational frequencies reaching approximately $0.995\omega_{\perp}$.
- The density profile of slowly rotating condensates differs very little from that of non-rotating condensates, except for the inclusion of the vortex cores.
- The Thomas–Fermi regime holds true for frequencies of $0.75 \leq \Omega \leq 0.99$, where kinetic energy remains negligible compared to flow velocity.
- The MFQH regime LLL description, holding for $0.99 \leq \Omega \leq 0.999$, sees the vortex cores expanding to fill all available condensate space. Density variation gives rise to energy terms of the order of flow velocity.

Following these statements, Fetter outlines some goals to observe effects and behaviours predicted to occur in rotating ultracold gas systems that still exist. Approaching and examining the behaviour of a condensate in the fractional quantum Hall regime, wherein ν is small, remains to be demonstrated. Rapidly rotating Fermi–gases are discussed also as an area requiring future investigation, and which may also provide insight into low ν states and behaviours.

1.2.5 Optical lattice potentials

Trapping potentials for Bose–Einstein condensates are typically harmonic, and are formed using magnetic (such as Ioffe–Pritchard) or optical potentials (such as dipole traps). Although these traps provide a single trapping location for all the atoms, interesting behaviour can also be observed and investigated using of an array of traps. One method of achieving this is the use of counter-propagating laser fields, allowing for a periodic optical potential to be created. For two sets of counter-propagating laser fields in a plane at right angles, an array of one-dimensional cigar-shaped condensate traps can be created, wherein the atoms are tightly confined in 2D. Adding an additional set of fields perpendicular to the existing ones will allow trapping of the atoms to periodic locations corresponding to a cubic lattice [? , chap. 2].

In 2002, the first realisation of a condensate trapped in a three-dimensional optical lattice was achieved by Greiner *et al.* [?]. They successfully realised an optical lattice in which the depth of the individual lattice sites could be adjusted by the intensity of the laser fields. By increasing the intensity from zero allows each site to obtain a number of condensate atoms. The authors show that increasing the intensity of the lattice lasers allows the system to move from a long-range phase coherent (BEC) state, to one where the phases between individual sites are no longer coherent, the so-called Mott insulator state. Such a system can no longer be described by a mean-field theory, and requires the use of a discrete quantum treatment, offered by the Bose–Hubbard model. To ensure the system remains in the ground-state, the intensity of the lattice potential was ramped to the required value slowly compared to the timescales for the

system to react. This ensured that no higher modes were excited, and allowed the condensate atoms to distribute amongst the trapping potential.

A theoretical investigation into the effect of optical lattices on vortex lattice structures was undertaken by Reijnders and Duine [?]. The authors were able to show that for in the presence of an optical potential which is not matched to the vortex lattice the vortices would break from an Abrikosov pattern, and become pinned to optical lattice sites. This was experimentally verified by Tung *et al.* [?]. They begin by comparing and contrasting pinned and Abrikosov vortex systems, and find that both allow “correlated many-body states” to be investigated. They consider competition between both lattice structures, and investigate the resulting behaviour of the condensate. Taking a 2D optical lattice superimposed upon the condensate in the fast rotation limit, the maxima of the optical potential create regions wherein it is energetically favourable for a vortex to sit. The authors show that a vortex may be pinned to a position given by the optical lattice, and through variation of the optical intensity a structural transition can occur from the triangular Abrikosov lattice to that of the optical lattice pattern. This is favoured when the two lattices rotate at the same rate, allowing the lattices to effectively “lock”. Using this technique the authors demonstrated a square lattice structure.

The use of optical lattices in combination with Bose–Einstein condensates in the manner described previously allows for many interesting effects unique to such systems. One such interesting body of theoretical work was that of Sørensen *et al.* [?], which involved the creation of FQH states, in a manner different from the fast-rotation route. The authors describe a process starting with a condensate in a harmonic potential in the Mott insulator state, going to the FQH state via the application of a magnetic field and reduction of the optical lattice potential, where the resulting state is in the LLL. A related work by Palmer *et al.* [?] investigates cold bosons in an optical lattice in the presence of large magnetic fields. The authors show that it is possible to generate FQH states, with varying fractional values. However, the proposed method is rather complex, and is described as requiring near future experimental technology to generate and observe such structures.

Another body of work investigating such behaviour was carried out by Vignolo *et al.* [?]. They investigate vortex dynamics in a condensate upon excitation by a 2D optical lattice. This theoretical study restricts itself to a single vortex, and can therefore be considered realisable using current state of the art technology [? ? ?]. Assuming a zero-temperature Bose gas, and a Bose–Hubbard Hamiltonian description, the authors derive a means of determining a vortex mass of the resulting system. This mass is stated as being easily tunable through variation of the confining potential along the rotation axis, assuming a pancake-shaped condensate. The use of Feshbach resonances [?] is also mentioned as a possible tool for altering the scattering length of the atoms, which provides a knob for the vortex mass to be adjusted. Through the use of Bragg scattering spectroscopic techniques, the authors state that in the presence of a vortex, the optical lattice structure exhibits a resonance allowing measurement of the vortex mass, which is absent when no vortex is present. The paper concludes by mentioning possible further studies, such as the case wherein interaction and tunnelling strengths are of the same order, or when many vortices are present within the system. These are stated to give rise to more complex system dynamics, and are, in the authors opinions,

experimentally realisable.

1.2.6 Recent advances and discoveries

There has been a significant amount of literature examining condensates with and without rotation and/or optical lattices, with both experimental and theoretical progress continuing in this area. The group of G. Campbell [?] examine the behaviour of a condensate in an annular trapping geometry, which is stirred by an optical potential barrier of varying intensity. Beginning with a stationary condensate, stirring was performed at a fixed rotational velocity using a repulsive potential barrier with diameter less than the trapping annulus width. Using the Thomas–Fermi approximation allowed for estimates of the chemical potential, μ , which in turn determined a value for the trap width and barrier width. Starting from zero intensity, the barrier was ramped to a maximum intensity over 100 ms, remained there for 800 ms and decreased over 100 ms. Following a time-of-flight expansion, excitations of the condensate were observed. Release of a non-rotating condensate shows the central hole of the condensate to close, resulting in a large peak at the centre. In contrast, a circulating condensate will show the presence of one or more holes, which signify “the presence of phase singularities (vortices)”. If a central hole is observed in the condensate density, the authors state that this is resulting from the presence of persistent currents in the condensate, which prior to release were flowing around the annular trap. The resulting diameter of the hole is dependent upon the winding number of the circulating current in the condensate. Holes that were reported as being off-centre show the presence of topological excitations (vortices) in the condensate. The authors show the probability of these excitations for a range of differing barrier heights and rotational frequencies, and attempt to formulate a theoretical framework to describe the results. Recognising that a full 3D model may be required to accurately describe the behaviour, the authors restrict themselves to a 1D approach, stating that ring-shaped geometries can be effectively treated as such. Although differences exist between experimental results and the theoretical approach taken the results were shown to agree qualitatively, where Campbell *et al.* suggest many possible reasons for such differences. This body of work represents some of the most recent experimental work on rotating condensates, and, as the authors have shown, requires further examination theoretically to accurately explain the results.

<!!!To be added -> results from NZ conference on arbitrary trapping potentials, automated BEC from C3QSI check over last 2 years for additional!!!>

With this section I have given an overview of theoretical and experimental results dealing with the superfluid behaviour of condensates.

Chapter 2

Numerics

2.1 Numerics

For many of the works described previously, it is necessary to apply numerical techniques to obtain results. As the Gross–Pitaevskii equation, given in Eq. (4.2), is used in the majority of the literature cited, we will consider it as the basis for the following discussion. Given the Gross–Pitaevskii equation, as defined by Eqn. 4.2, we can see that it is a second order non-linear partial differential equation. Very few exact solutions exist, and the problem must often be tackled by a numerical approach. Though there are many ways to solve such a system numerically, (such as Crank-Nicholson, Trotter-Suzuki), the method I have chosen is the pseudospectral Fourier split-operator [?].

If we consider a unitary evolution operator of the form

$$\Psi(\bar{x}, t + \tau) = \exp \left[-\frac{iH\tau}{\hbar} \right] \Psi(\bar{x}, t), \quad (2.1)$$

where H is the Hamiltonian, composed of momentum, potential, non-linear, and rotation terms defined in Eq. (4.2), we can solve for the wavefunction over a specified timescale. However, due to error propagation resulting from numerical integration techniques, it is necessary to employ methods that allow for the highest precision while providing results in useful timescales. To allow for this, careful choice of the numerical integration methods must be taken. If we take the Hamiltonian, H , in terms of its components as a combination of position and momentum space functions we obtain

$$\hat{H} = \hat{H}_{\mathbf{r}} + \hat{H}_{\mathbf{p}} + \hat{H}_{\mathbf{L}}, \quad (2.2)$$

where we first neglect the angular momentum operator, $\hat{H}_{\mathbf{L}}$, and consider only the two other non-commuting parts $\hat{H}_{\mathbf{r}}$, containing the position operator, and $\hat{H}_{\mathbf{p}}$, containing the momentum operator. This way we can reduce the error in the numerical integration scheme by using 2nd order Strang-splitting as

$$\exp \left[-\frac{i \left(\hat{H}_{\mathbf{r}} + \hat{H}_{\mathbf{p}} \right) \tau}{\hbar} \right] \approx \exp \left[-\frac{i\hat{H}_{\mathbf{r}}\tau}{2\hbar} \right] \exp \left[-\frac{i\hat{H}_{\mathbf{p}}\tau}{\hbar} \right] \exp \left[-\frac{i\hat{H}_{\mathbf{r}}\tau}{2\hbar} \right]. \quad (2.3)$$

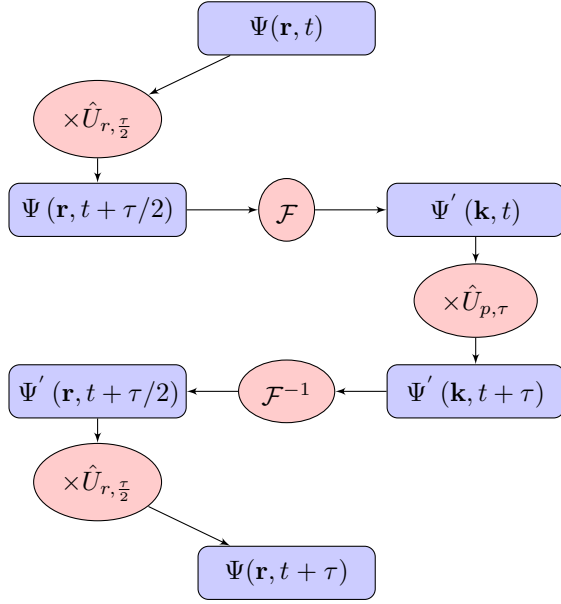


Figure 2.1: A single pass through the Fourier split-operator method.

The respective functions can be mapped to the Gross–Pitaevskii equation’s position, and momentum terms as

$$\hat{H}_{\mathbf{r}} = V(\bar{x}) + g|\Psi(\bar{x}, t)|^2 \quad \hat{H}_{\mathbf{p}} = \frac{-\hbar^2}{2m} \nabla^2. \quad (2.4)$$

Following Bauke *et al.* [?], we can numerically solve this differential equation as

$$\Psi(\mathbf{r}, t + \tau) = \left[\hat{U}_{\mathbf{r}} \left(t + \frac{\tau}{2} \right) \mathcal{F}^{-1} \left[\hat{U}_{\mathbf{k}}(t + \tau) \mathcal{F} \left[\hat{U}_{\mathbf{r}} \left(t + \frac{\tau}{2} \right) \Psi(\mathbf{r}, t) \right] \right] \right] + O(\tau^3), \quad (2.5)$$

where $\hat{U}_{\mathbf{r}} = e^{-i\hat{H}_{\mathbf{r}}(t)\tau/\hbar}$ is the time evolution operator in real space, $\hat{U}_{\mathbf{p}} = e^{-i\hat{H}_{\mathbf{p}}(t)\tau/\hbar}$ in momentum space, \mathcal{F} and \mathcal{F}^{-1} are the forward and backwards Fourier transform respectively. Following [?] and taking the Madelung transform of the wavefunction given by Eq. (1.32), the phase of the condensate may be given by

$$\theta = \theta_c + \theta_i, \quad (2.6)$$

where θ_c is the unperturbed condensate phase, and θ_i is the phase pattern to be imprinted. Thus, upon solving for the initial condensate phase, an additional phase pattern can be imprinted at any time by multiplying the wavefunction by the intended phase pattern. This is in line with the phase imprinting method, as previously introduced by Dobrek *et al.* [?]. The underlying theory of the Fourier split-operator method for the Gross–Pitaevskii equation is given by Javanainen *et al.* [?], showing how the choice of non-linearity and operator splitting affects the outcome of the method. The authors arrive at the conclusion that treating the non-linearity and potential terms together with the most current wavefunction definition yields results with an error magnitude that matches those obtained in the Schrödinger Fourier split-operator case, indicating its applicability to this type of problem.

2.2 Angular momentum operators using FSO method

The Fourier split-operator method described earlier works well in handling cases where the operators live in position or momentum space respectively. However, the angular momentum operators are essentially a combination of both spaces as we deal with each basis respectively. Take, for example, the angular momentum operator along the z -axis, given by $L_z = xp_y - yp_x$. To apply L_z we must take not that the x and y components of the wavefunction must be in alternating bases for the evolution. Thus, to apply this operator we must Fourier transform along a single dimension, multiply by the respective operator, take the inverse, and perform this operation along the other dimension.

This, however, accrues an error not encountered using non-pseudospectral methods. The error can be determined by checking the commutativity of the respective components of the angular momentum operator as

$$L_1 = [xp_y, -yp_x] = [xp_y, -y]p_x - y[xp_y, p_x], \quad (2.7)$$

$$= -[-y, xp_y]p_x + y[p_x, xp_y], \quad (2.8)$$

$$= -\left(\overbrace{[-y, x]p_y}^0 + x[-y, p_y]\right)p_x + y\left(\overbrace{[p_x, x]p_y}^0 + x\overbrace{[p_x, p_y]}^0\right), \quad (2.9)$$

$$= -x\overbrace{[-y, p_y]p_x}^{i\hbar} + y\overbrace{[p_x, x]p_y}^{-i\hbar}, \quad (2.10)$$

$$= -i\hbar(xp_x + yp_y). \quad (2.11)$$

The complex error term can be seen as, in the case of the implemented evolution, allowing the angular momentum operator to change from imaginary time to real-time, and vice-versa in each respective case. To overcome this, we simply swap the application order of the operator components, between even and odd steps during the evolution. Starting with the alternate order we obtain a value of $L_2 = [-yp_x, xp_y] = i\hbar(xp_x + yp_y)$. Since we are applying this phase to the condensate we can overcome the error of one term by the application of the other, as

$$\exp iL_1 \exp iL_2 = 1. \quad (2.12)$$

Although alternating will provide a cancellation of this error, it can be assumed that for large timesteps the error will have a non-insignificant contribution to the overall dynamics. Thus, for this method to remain accurate we can perform the previous decomposition for a third-order accurate scheme, or use as is for a second-order accurate scheme.

2.2.1 Time evolution

To create the initial state for the desired evolution the ground-state of the Hamiltonian needs to be determined as a first step. This can be achieved by evolving the system in imaginary time, where $t \rightarrow it$. This causes all higher energy terms in an initial guess for the condensate wavefunction to decay to zero, leaving the lowest energy state, which corresponds to the ground-state. As effective as this approach may be, the convergence to the lowest lying energy state becomes less effective as the computation approaches

the expected value [?]. Although many such methods exist, the one that is best suited for this task is that of a Fourier split-operator method. Due to the way the algorithm operates, it is essential to have a large and finely sampled grid in order to resolve both position and momentum of the wavefunction. A minimum grid-size on the order of 2^8 in 2D for both X and Y dimensions is required. An implementation of such a method at the defined resolution is a straight-forward process using MATLAB, and has been performed for the purpose of this study. However, due to the large computational overhead required to deal with such a calculation, the procedure takes a long time to evolve the system to the necessary degree of accuracy. Therefore, it is necessary to further develop the methods used, and to improve the implementation of this algorithm to leverage the recent advances in computational acceleration.

We can write the wavefunction of a quantum system as a linear superposition of states as

$$|\Psi\rangle = \sum_n C_n |\Psi_n\rangle, \quad (2.13)$$

where $|\Psi_n\rangle$ are a set of basis states for the system, with complex coefficients C_n . We next assume a unitary evolution operator of the form

$$\mathcal{U}(t, t_0) = \exp\left(\frac{-i\mathcal{H}(t - t_0)}{\hbar}\right), \quad (2.14)$$

where \mathcal{H} is the Hamiltonian of the system. To time evolve our system from some time t_0 to a final time t we apply the evolution operator to the wavefunction, giving

$$\mathcal{U}(t, t_0)|\Psi\rangle = \sum_n C_n \exp\left(\frac{-iE_n(t - t_0)}{\hbar}\right) |\Psi_n\rangle, \quad (2.15)$$

where I have replaced the Hamiltonian operator with the energy eigenvalue of the n -th state. It follows from here that each state evolves at a different rate, proportional to its given eigenenergy. Higher energy states will oscillate faster than those of lower energy states. However, to make accurate predictions it is often necessary to deal with a single quantum state, such as the lowest lying state. We can learn much from a quantum system's lowest energy state, and so to evaluate this would be very useful. Taking the evolution operator, we apply a Wick rotation, rotating the time component through $\pi/2$ into the imaginary plane, as $t \rightarrow -it$. Applying this new evolution operator to the wavefunction gives

$$\mathcal{U}'(t, t_0)|\Psi\rangle = \sum_n C_n \exp\left(\frac{-E_n(t - t_0)}{\hbar}\right) |\Psi_n\rangle. \quad (2.16)$$

The we have removed the complex term in the operator, which now takes the form of an exponentially decaying operator. When applied to the wavefunction all higher energy terms will decay at a rate faster than lower energy components. This process also causes a loss of probability density, and so the wavefunction must be renormalised after application. Through repeated application of this operator, and a renormalisation afterwards, the quantum system can converge to the groundstate. To begin, however, we must assume an initial guess for the wavefunction, which has some finite overlap with the lowest lying state.

2.3 Vortex tracking

To efficiently follow the vortex dynamics, some robust algorithm is needed to track their positions. We could track regions where the density drops to zero. However, this gives very little information on the topological excitation, and may mistake density dips for the presence of such excitations. Thus, one of the most effective ways is to locate the $\pm 2\pi$ charge in the wavefunction phase, which is a signature of quantum vortices. For this, we can assume that around a 2×2 subgrid, the phase rotates from $-\pi$ to $+\pi$ in the presence of a vortex located on the subgrid. After an initial pass to determine the vortex locations closest to the nearest grid element, a least-squares fit is performed to more accurately determine the vortex core position. With this, we can accurately determine the motion of the vortices with high precision.

To track the vortices during the evolution, the creation of an initial list of vortices is performed, with each given a unique identifier. Assuming the vortex cores can travel a limited distance (some multiple of the grid resolution) between time steps, we can say at subsequent times which vortex has moved to the newly found positions. This is performed through use of a linked list of vortices, each with an assigned unique identifier, associated location, phase winding and on/off flag. A finite boundary is chosen to examine only vortices at the center, which can cause vortices to appear and disappear on the boundary. Thus, any vortex which appears without association to an initial vortex, or any vortex that leaves the boundary, is switched off and remains so for all analysis.

2.4 General purpose GPU computing

As the dimensionality of a problem increases, so often too does the time required for performing simulations. It can become necessary to find ways of optimising the use of computational resources to reach a final result in a much shorter amount of time. One such method for accelerating numerical solutions involves the use of multiple compute cores on a central processing unit (CPU) operating independently on different data elements in unison. This form of parallel computation can be achieved through the use of the OpenMP (Open Multi-Processing) application programming interface (API), which defines how a program may parallelise certain elements of code. It allows the developer to fully utilise the power of a multicore processor. However, the limit on how much performance can be gained by this method is set by the number of compute cores available to the system. It should also be noted that MATLAB has inherent support for such programming paradigms, and fully abstracts the implementation from the developer. Therefore, in this instance using such a means of parallelisation would not be very beneficial <!!!why not?!!!>.

Another widely used programming paradigm is that of MPI (message passing interface). Where OpenMP allows a user to utilise all available processors on a single system, MPI allows the use of an (almost) unlimited number of computer systems operating in parallel together, each known as a node. This is the method generally preferred in programs written for compute clusters, where a large number of nodes are available to use. It is preferable for applications that have minimal dependence between

data, as a compute bottleneck may occur if data spread over multiple nodes is required for an operation. This would require continual transmission of data between individual nodes, which (at current data rates) would be limited to bus speeds of (assuming Infiniband optical connections) on the order of ten gigabytes per second. Compared to a local calculation requiring little to no transfers, the memory bandwidth can be (assuming current high performance 12 core processors) as high as 60 gigabytes per second [?]. Therefore, it is important to note that transfers should be minimised to avoid bottlenecks, but transfers are often necessary to make use of the large number of processing cores required to obtain results within short timescales. Therefore, to give a significant performance benefit, a large number of cores, a high memory bandwidth, a high-speed interconnect between cores (nodes), as well as sufficient space to store the problem in memory are required.

One possible means of achieving this high performance is through the use of graphics processing units (GPUs). GPUs are signal processing devices, and have been highly developed over the past 20 years to offload much of the computation required to display images from the central processing unit (CPU). As a result, GPUs have been given the task of performing operations necessary to update a large number of pixels in a short amount of time, as well complex 3D math for image rendering. This has been achieved through giving the GPUs a large number of specialised compute cores for floating-point arithmetic, effectively operating in parallel. With the advent of general purpose GPU (GPGPU) computing, the ability to exploit these cores for the purpose of numerical computing has become possible. A problem can be mapped to the hardware of a GPU, and all parallelisable operations can be accelerated, reducing the overall compute overhead required for evaluating results. For the latest generation of industry standard GPUs used in computational acceleration the memory bandwidth for the device global memory (equivalent of RAM) is given as 288 gigabytes per second, with almost 3000 cores on demand, yielding a total of 1.41×10^{12} <!!! where do you calculate this?!!!> floating-point operations per second (FLOPS). In comparison to this are Intel Xeon CPU throughput values, which yield approximately 1×10^{11} FLOPS. As can be seen, performance of an order of magnitude can be gained by using a GPU for calculations, over high-performance (Xeon) CPUs. This has been shown to allow for effective implementation of the previously mentioned Fourier split-operator method [?], and we have shown that it yields performance exceeding that of CPU's for a modest choice of GPU [?].

2.5 GPUE: GPU Gross–Pitaevskii equation solver

As mentioned previously, the split operator method makes use of Fourier transforms as a way to change between position space and momentum space. To speed this up, the GPU accelerated CUFFT library is used, allowing for a much faster FFT than can be performed on a single (or across multiple) traditional CPU nodes. However, to take advantage of the GPUs performance, it is essential to minimise the data transfer between host machine (CPU) and device (GPU). Therefore, the remaining operations for the evolution must also be carried out on the GPU. This also requires that the workload is evenly distributed across the cores on the GPU so that we minimise the

number of threads that are not performing computations.

Given that the problem of simulating the GPE in a rapidly rotating regime can be modeled as two-dimensional, we can put a limit on the

2.5.1 Introduction

Recent experimental progress in trapping and controlling all degrees of freedom of single atoms and ions has allowed us to test and explore the fundamentals of quantum mechanics at a completely new level [? ?]. In fact, progress has been so dramatic that application of the laws of single and few particle quantum mechanics to areas such as quantum information and quantum metrology has come into experimental reach [? ?].

While control over the internal degrees of freedom of atoms is a highly advanced field, significant progress in developing techniques to coherently control the external degrees of freedom to the same level has only recently been achieved. One class of techniques that can offer high fidelities are adiabatic processes and recently a technique called Coherent Tunnelling by Adiabatic Passage (CTAP) was shown to be a very promising tool for controlling the quantised centre-of-mass state of a single particle trapped in a microtrap [?]. CTAP is designed to transfer populations between microtraps at high fidelities while being robust to variations in the system parameters. Although the physics of CTAP is well understood, the process has yet to be observed experimentally and several realistic systems have recently been proposed [? ? ?].

Coherent transport between microtraps can be facilitated via tunnelling and the tunnelling rates can be controlled by moving the centres of the individual traps relative to each other. While this requires dynamical potentials, a similar system with static potentials can be constructed by considering three parallel running waveguides with spatially varying coupling strength between them and an atom which travels along these guides [?]. Recently, in our previous work, a realistic atom chip system of this kind was considered [?], however the simulations were limited to two dimensions.

While the transversal dynamics in a system of waveguides can be well described in a two-dimensional model, effects stemming from bending, longitudinal dispersion and the lack of stationary states in the z -direction cannot be accounted for. To overcome these limitations and understand the total dynamics of a waveguide system, it is necessary to carry out a fully three dimensional simulations.

We therefore present here, an analysis of a system composed of three waveguides by taking the full dynamics in all three spatial directions into account and using realistic experimental parameters. The latter is important as most treatments of the problem in recent years have assumed idealized trapping potentials that guarantee resonance between the individual traps at any moment in time. By carrying out three dimensional simulations which account for all possible dynamics, we show that CTAP is indeed a suitable technique for use in waveguides on atom chips.

By today, fully three dimensional simulations of the Schrödinger equation in the context of atomic transport are still rare [?]. The computational resources needed are very large and have traditionally required the power of large supercomputers. Recently it was shown that the emerging technique of GPU (graphics processing unit) computing allows tremendous speedup of many numerical techniques including the fast Fourier

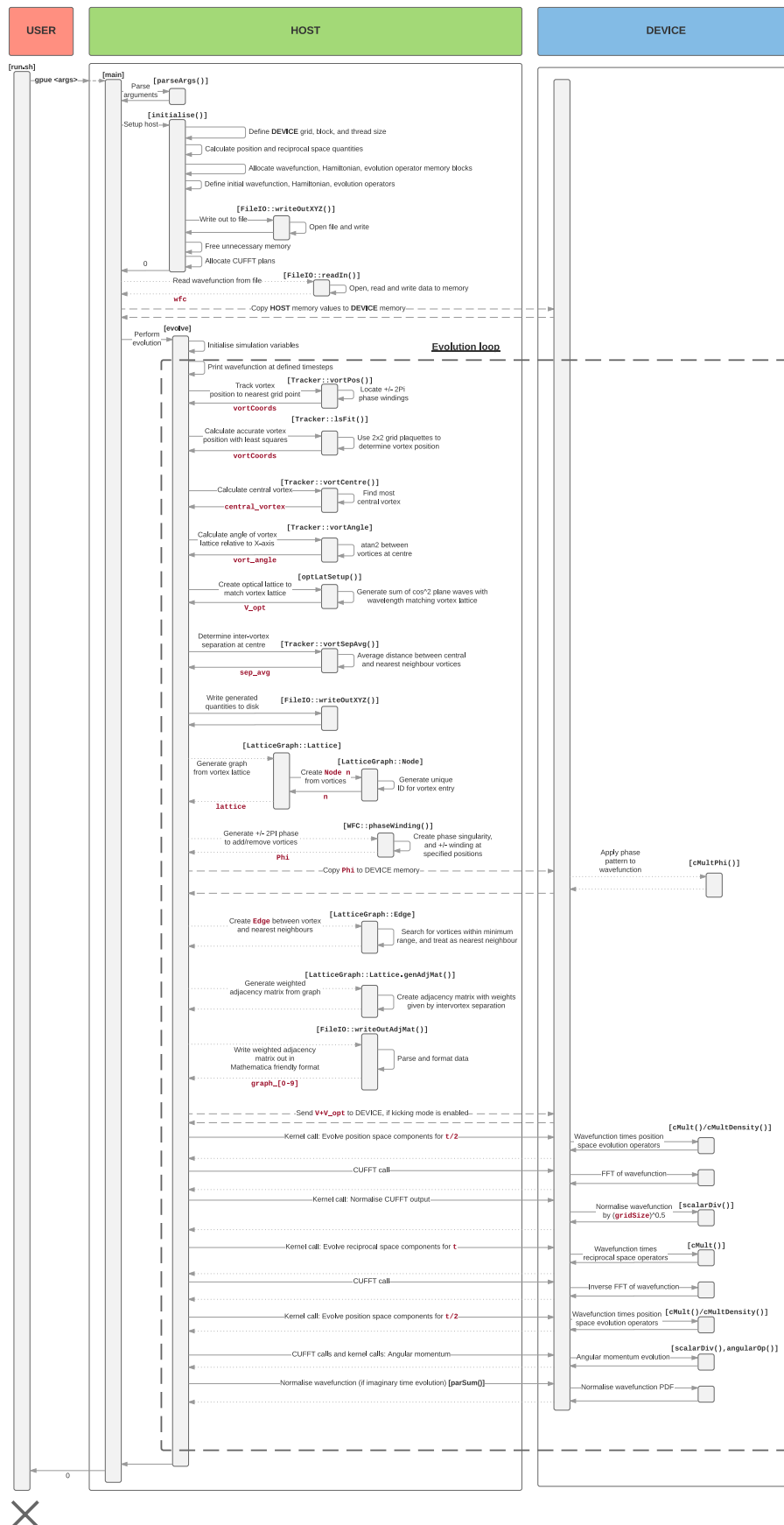


Figure 2.2: Simplified combined sequence and state diagram for GPUE operation.

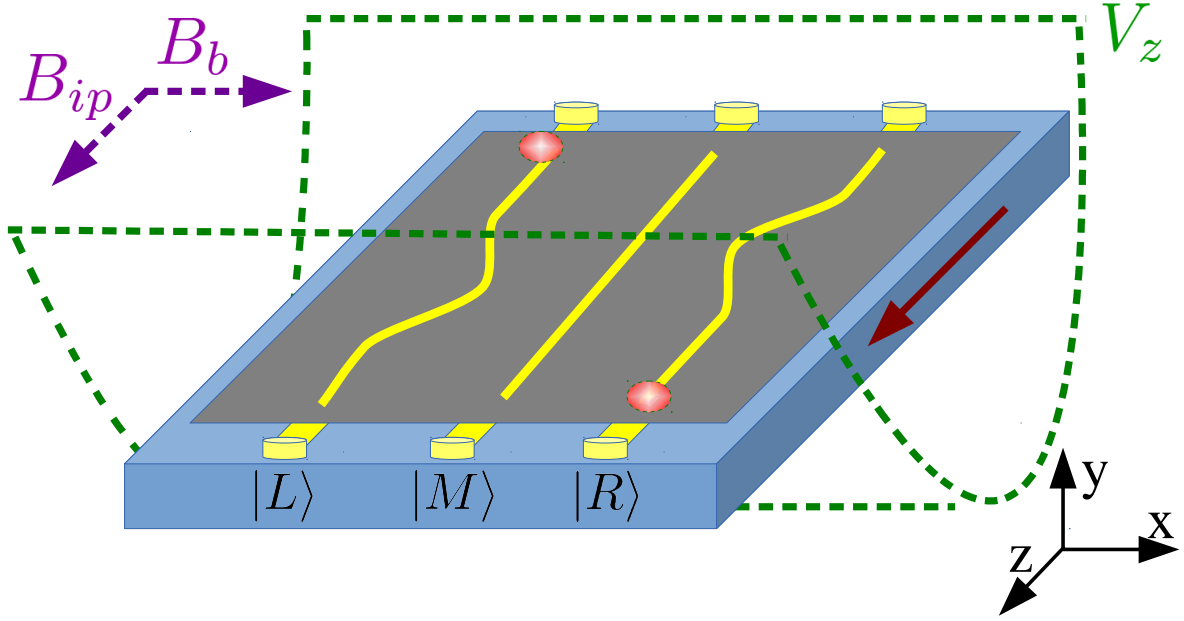


Figure 2.3: (Color online) Schematic of the suggested setup for observing the CTAP process in a system of waveguides. Note that the asymmetric approach of the outer wires to the middle wire is exaggerated, so that the counter-intuitive arrangement is visible. The atom is initially located in the left guide and, due to the presence of a harmonic oscillator potential V_z in the z -direction, travels along the direction indicated by the red solid arrow. We also show the expected position of the atom at $t = \pi/\omega_z$ in the right hand side guide and indicate the orientation of the bias field, B_b , and the applied field, B_{ip} (purple dashed arrows).

transform (FFT) [?], which is the main numerical tool that we require. By making use of this, we have been able to perform the simulations of this extensive atomic system with one consumer desktop PC using the CUDA programming model and numerical libraries, on very reasonable timescales.

The structure of this paper is as follow. In Sec. 2.5.2 we will briefly review the CTAP process in waveguide systems and in Sec. 2.5.3 we describe the atom chip potentials we are simulating. In Sec. 2.5.4 we will discuss our implementation of CUDA and MPI (Message Passing Interface) codes and examine the performance benefits in each case. Our results of the three dimensional simulations and the evidence that CTAP can be observed will be presented and discussed in Sec. 2.5.5. Finally we conclude in Sec. 2.5.6.

2.5.2 Coherent Tunnelling by Adiabatic Passage

Let us first briefly review the CTAP process by considering an atom trapped in a linear system of three identical, one-dimensional microtraps [?]. Assuming that the atom is in its centre-of-mass ground state in the trap on the left hand side, $|L\rangle$, it can reach the ground states of the other two traps, $|M\rangle$ and $|R\rangle$, through coherent tunnelling described by the strength J_{LM} for the transition $|L\rangle \rightarrow |M\rangle$ and J_{MR} for $|M\rangle \rightarrow |R\rangle$.

In this basis the Hamiltonian is given by

$$H(t) = \hbar \begin{pmatrix} 0 & -J_{LM}(t) & 0 \\ -J_{LM}(t) & 0 & -J_{MR}(t) \\ 0 & -J_{MR}(t) & 0 \end{pmatrix}, \quad (2.17)$$

where the energy of the trap ground states was re-normalized to zero. The tunnelling strengths are assumed to be time-dependent, which can be achieved by increasing or decreasing the distances between neighbouring traps, $d_{LM}(t)$ and $d_{MR}(t)$. The eigenstates of the Hamiltonian (2.17) are well known [?] and of particular interest for adiabatic transport is the so-called dark state

$$|d\rangle = \cos \theta |L\rangle - \sin \theta |R\rangle, \quad (2.18)$$

in which the mixing angle θ is given as a function of the tunnelling strengths as

$$\tan \theta = J_{LM}/J_{MR}. \quad (2.19)$$

This state has a non-degenerate zero eigenvalue and an adiabatic evolution will therefore guarantee that the system, once prepared in $|d\rangle$, will always stay in it. Note that the only contribution of $|M\rangle$ to $|d\rangle$ is through the mixing angle and that the system has zero probability to be found in $|M\rangle$ at any time.

The CTAP process can now be understood by considering an atom initially in the state $|L\rangle$. Increasing and decreasing J_{MR} before J_{LM} , which is counter-intuitive to traditional tunnelling schemes, continuously decreases the population in state $|L\rangle$ and increases the population in state $|R\rangle$, leading to a 100% transfer at the end of the process.

Adapting this process to a system of waveguides is now straightforward. The temporal dependence of the tunnelling strength in eq. (2.17) can be replaced by a spatial one through suitable adjustment of the distance between neighbouring waveguides as a function of the direction the particle travels in (see Fig. 2.3 for a schematic view) [?].

There are, however, several conditions that both, the microtrap and the waveguide system, must fulfil for the CTAP dynamics to occur. Firstly, the process must be adiabatic with respect to the other relevant energy scales in the system. For the waveguide system this means the whole process has to be slower than the inverse of the approximate transverse trapping frequencies of the guides. As typical numbers for such guides are in the kHz regime, this means that the time allowed for the atom to travel along the chip can be much shorter than a typical system's lifetime. The second condition which has to be fulfilled, as previously mentioned, is that all trapping states are in resonance at any point in time, which is difficult to achieve once the potentials of the individual guides start to overlap. However, we will demonstrate in the next section how a waveguide setup on an atom chip is a realistic experimental system in which this resonance condition can be fulfilled to a good approximation.

2.5.3 Atom Chips

Atom chips are versatile experimental tools that are by today used extensively in experiments with ultra-cold atoms [? ?]. A small current flowing through nano-fabricated wires on the substrate produces a magnetic field gradient in such a way, that

cold atoms can be trapped very close to the surface. Because the layout of the nanowires can be chosen during the chip’s production process, atom chips have been used in many cold atom experiments to produce microtraps, interferometers and waveguides [? ? ? ?]. Here we will take advantage of this versatility to consider waveguides in the geometry indicated in Fig. 2.3 and develop a procedure which will allow to observe high fidelity transport based on CTAP.

Let us briefly review the basic description and properties of atom chip trapping. The magnetic potential \mathbf{B} at position \mathbf{r} generated by a typical nanowire on an atom chip can be described by the Biot-Savart law

$$\mathbf{B} = \frac{\mu_0 I}{4\pi} \oint \frac{d\mathbf{l} \times \hat{\mathbf{r}}}{r^2}, \quad (2.20)$$

where I is the current in the wire, μ_0 the vacuum permeability, $\hat{\mathbf{r}}$ the unit vector in the direction of \mathbf{r} and $d\mathbf{l}$ is the differential length of the wire carrying current I . For this expression to be valid, however, we have to assume that the thickness of the wires is negligible, which is a good approximation as long as we are using the properties of the field at a sufficient distance above the chip’s surface. To achieve this and to lift the field minima above the nanowires for the desired waveguide structure, a homogeneous magnetic bias field, B_b , can be applied orthogonal to the current flow. This raises the potential minimum to a height above the wire given by

$$r_0 = \frac{\mu_0}{2\pi} \frac{I}{B_b}. \quad (2.21)$$

Finally, to lift the degeneracy of the spin states of the atoms and avoid losses due to spin flips at the centre of the waveguide a further magnetic field, B_{ip} , parallel to the direction of the wires is usually applied.

An example of the waveguide potentials resulting from this model for ^6Li atoms and for experimentally realistic parameters is shown in Fig. 2.4. If an atom is initially located in the left waveguide and travels in the positive z -direction, these waveguides provide the desired counter-intuitive tunnel coupling needed for CTAP. To give the atom momentum to travel along the wires we add an additional harmonic oscillator potential, V_z , of frequency ω_z along the z -direction, which is centred at the middle of the chip (see Fig. 2.3). This will also lead to a re-focusing of the travelling wavepacket at the classical turning point on the other side of the chip and help to clearly determine the position of the atom.

To ensure that the process is adiabatic and the atom remains in the dark state of the system at all times, the total time for the process has to be much larger than the inverse of the transverse trapping frequencies of the individual waveguides. By approximating the potentials to have a harmonic oscillator shape in the transverse direction, we find the inverse of the relevant frequency to be of the order of $f_{HO}^{-1} \approx 0.2$ ms and by choosing the trapping frequency of the harmonic oscillator in the z -direction to be $\omega_z = 2\pi \times 5$ Hz, the total time taken for the process (half an oscillation) is 0.1 s. This allows to clearly fulfill the adiabaticity condition at any point during the evolution.

Finally, the bend in the wires will lead to a potential from the currents in the z -direction, which requires the atom to have enough kinetic energy to overcome it and therefore sets an upper bound to the adiabaticity that can be reached. However,

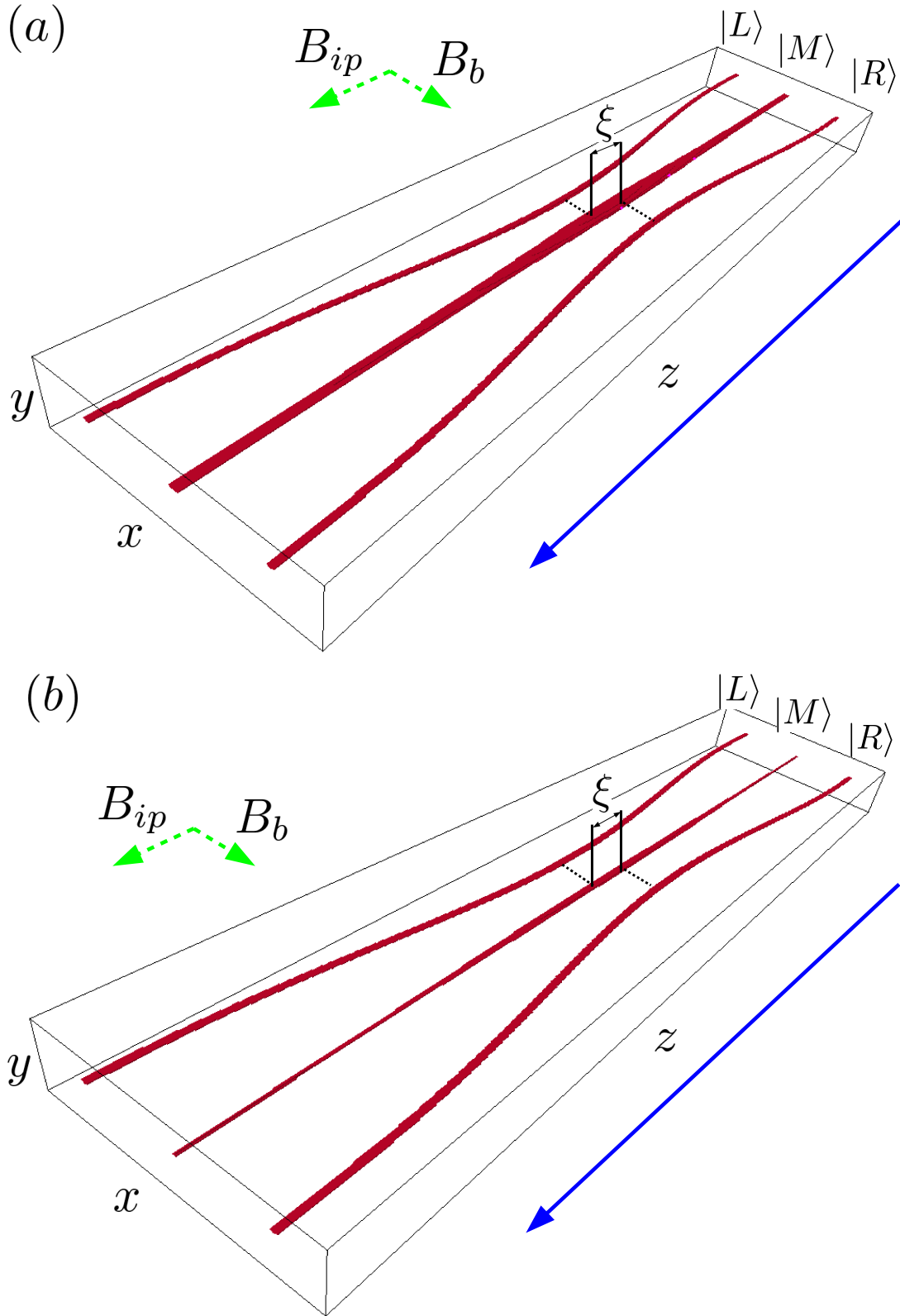


Figure 2.4: (Color online) Isosurfaces of the waveguides created on an atom chip with the direction of propagation indicated by the blue solid arrow (for clarity $V_z = 0$ in this plot). The dimensions of the interesting area on the chip we simulate are $20\mu\text{m} \times 1000\mu\text{m}$ ($x \times z$) and we take a height (y direction) above the chip of $4\mu\text{m}$ into account. The three wires are initially equally separated by $7\mu\text{m}$ and their distance at the position

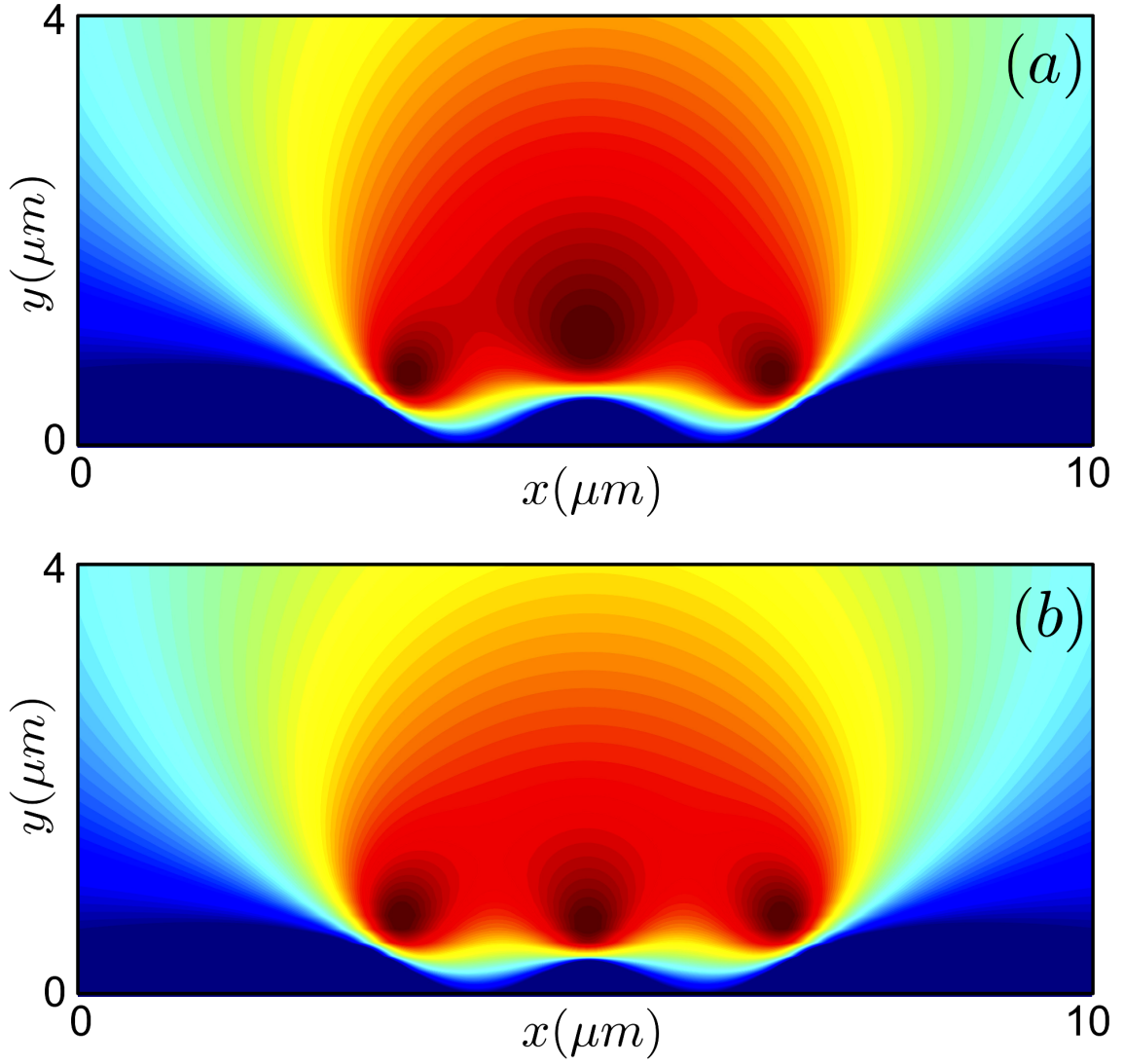


Figure 2.5: (Color online) Contour plot of the waveguides at $500\mu m$ along the z -axis. Panel (a) shows the deformation of the waveguides when all currents are equal, $I_L = I_M = I_R = 0.1A$ and panel (b) shows how this effect can be mitigated by using a reduced middle wire current of $I_M = 0.07A$, while the current in the outer wires remain at $I_L = I_R = 0.1A$.

this effect can be reduced by increasing the length of the atom chip (z -direction) and therefore reducing the curvature of the wires. From our simulations, we find that the kinetic energy resulting from locating an atom initially at the edge of a chip that is $z_{max} = 1000\mu\text{m}$ long allows us to successfully propagate the atom through the waveguides using the harmonic trap described above.

2.5.4 MPI and CUDA

To simulate the propagation of the atom along the waveguide we solve the three-dimensional time-dependent Schrödinger equation using the well known Fourier Split Operator method [?]. A typical numerical implementation of this method requires the use of 4 Fourier transforms followed by 3 complex multiplications for each time step. The numerical library we make use of to perform the Fourier transforms is the well known FFTW library, and its GPU implementation CUFFT [?].

Performing three dimensional Fourier transforms is the most intensive part of our code with the length of time required to perform one iteration of the split operator method depending heavily upon the size of the numerical grid. As discussed in the previous section, the atom chip has a relatively large extension in the z -direction ($z_{max} = 1000\mu\text{m}$) compared to the other dimensions. Since the maximum value of the momentum grid is defined as $p_{max} = \frac{\pi N_z}{z_{max}}$ we require a large number of points, N_z , for our grid to be large enough to resolve the longitudinal momentum stemming from the external harmonic oscillator potential. This is the main reason that the computational resources required to simulate the system are quite substantial.

GPU Computing

To overcome the numerical barrier presented by this system we turn to the relatively new computing paradigm of GPU (graphics processing unit) computing. Whereas traditional computers perform computations using the central processing unit (CPU), GPU computing allows some of the work to be offloaded to the graphics processor. GPUs are inherently SIMD (single instruction, multiple data) devices, designed for operating upon a large data set at a given time with a single task, such as a 2D grid of pixels. Due to their parallel nature, GPUs can perform better than CPUs for certain types of calculations. One example where they offer large performance gains are fast Fourier transformations (FFTs) and it was recently shown that the Fourier split operator method can be accelerated using GPU computation [?]. This performance increase offers the numerical power needed to simulate the above system and we have implemented the algorithms for split-operator evolution of the Schrödinger equation with C, CUDA and Nvidia's CUFFT libraries for the Fourier transforms.

Performance

To demonstrate the performance offered by GPU computing we compare it to using FFTW with MPI, a more traditional CPU-based method. The message passing interface (MPI) implementation allows the code to be run across multiple machines,

Device	Num. Devices	Timing	Rel. Improvement
CPU (MPI)	8	~6 Hr	1.0×
	16	~4 Hr	1.5×
	32	~1.5 Hr	4.0×
	64	~1 Hr	6.0×
GPU	1	~1 Hr	6.0×

Table 2.1: The approximate times taken to simulate the propagation of an atom through our atom chip system on both GPU and CPU.

benefiting from the parallelism which may be offered by a supercomputing cluster. Although MPI-enabled FFTW is fast and supports extremely large grid sizes, it requires computer-cluster access of a significant size to be a viable option.

To effectively simulate the CTAP process and accurately resolve the momentum, our code requires a grid size of $256 \times 64 \times 1024$ ($x \times y \times z$). For accurate time evolution a timestep of $\Delta t = 1 \times 10^{-6}$ s was found to be adequate. For the GPU simulations, the test system was an Intel Core i7 2600K CPU at stock frequency, 8GB DDR3 memory operating at 1600 MHz, 7200 RPM HDD, Nvidia GeForce GTX 580 with 3GB of onboard memory running at 783 MHz GPU core frequency, 1566 MHz shader processor frequency, and 2010 MHz memory frequency. For all simulations the desktop was running Ubuntu 11.10 64-bit operating system and all calculations were performed in double precision (64-bit floating point) where applicable. For the CPU simulations we utilized the supercomputers at ICHEC (Irish Centre of High-End Computing).

Table 2.1 shows the approximate timings for the completion of runs on GPU and CPU. As one can see, not only does GPU computing offer a 6-fold improvement over a single CPU, it also allows us to achieve a performance level which is comparable to a 64 core CPU. Such performance has previously been restricted to high powered supercomputers. Having such computational power available to a single user on a Desktop computer allows us to obtain a large volume of simulated data on a much shorter timescale rather than through the use of a shared resource CPU-based computer cluster. Additionally, a second GPU card added to the system allowed concurrent runs of the code, which effectively halved the overall time required for a large number of simulations. It is also worth mentioning that moving computations over to the GPU of the system frees up the CPU and a large part of the system memory to be used for other task that would have previously been inhibited by CPU bound computations.

2.5.5 3D Simulations

In the following section we will present a set of typical results from the GPU accelerated 3D simulations we have carried out over a large range of experimentally controllable parameters and show that the atom chip allows for the CTAP process to take place. All parameters for our atom chip are the same as in Fig. 2.4 unless otherwise stated.

Our simulations start out with a single ${}^6\text{Li}$ atom which is initially located in the left waveguide. Its transversal wavefunction corresponds to the ground state of the potential in the transversal direction (determined numerically) and longitudinally we

assume a Gaussian profile of similar width. We then evolve this initial state in time and due to the longitudinal harmonic oscillator potential centred at the middle of the atom chip ($z = 500\mu\text{m}$), the atom starts to propagate along the waveguide.

Initially the wires are far enough away from each other for each waveguide to be approximately given by the current of the wire closest to it and if all currents are identical, the waveguides are in resonance. However, once the wires start approaching each other, the respective magnetic fields add and create waveguide potentials of unequal size (see Figs. 2.4 (a) and 2.5 (a)). This drives the transversal ground states of the guides out of resonance and the conditions for observing the CTAP process are no longer given.

However, atom chips offer an intriguingly straightforward way to adjust for this, as the current in each wire can be individually (and even time-dependently) controlled. This can be used to compensate for effects stemming from the potentials overlapping and ensure resonance between the waveguides [?]. While one can imagine a numerically optimised algorithm that adjusts the currents in a time-dependent manner based on the position of the centre-of-mass of the atom, here we will show that a much simpler approach, which maintains the simplicity of all currents being constant in time, is already sufficient. We suggest to reduce the current in the middle wire so that in the crucial coupling region, where the magnetic fields from neighbouring waveguides have the strongest influence on each other, the waveguides are approximately resonant.

To demonstrate the effect of this adjustment we show in Fig. 2.5 a transversal cut through the system at the middle of the chip ($z = 500\mu\text{m}$) for the case where (a) all three currents are identical ($I = 0.1\text{A}$) and (b) where the current in the middle wire is reduced ($I_M = 0.07\text{A}$). One can clearly see that the transversal shape of the waveguides is very similar for the case of the reduced centre current, which indicates that this approach can lead to enhanced resonance between the guides.

In the areas where the guides are further away from each other, however, the reduced current in the middle wire will have the opposite effect and reduce the quality of the resonance. This can clearly be seen from the iso-potential surface plot in Fig. 2.4 (b). Yet, since the tunnelling in these areas is small, it has only a negligible influence on the CTAP process and we will in the following demonstrate that the near resonant setup of Fig. 2.5 (b) allows to observe the CTAP process.

In Fig. 2.6 we show the population in each waveguide as a function of time for an atom chip with reduced current in the central wire. The results in Fig. 2.6 (a) are obtained for the situations where the wires are arranged such that the counterintuitive tunnelling sequence takes place and full transfer from the initial guide into the final guide is clearly visible. Only a small population in the central guide appears halfway through the process, and while the ideal CTAP process does not allow for population in the central trap at any time, the limited adiabaticity and resonance of the simulated setup leads to this temporary deviation. However, it has no effect on the final state.

In contrast to this, and confirming that the large fidelity of the transport process above is due to CTAP, we show in Fig. 2.6 (b) the results for an intuitive arrangement of the waveguides on the atom chip. As is clearly visible, this does not produce high fidelity population transfer to the guide on the right hand side, but rather leads to a split of the probability between the middle and the right hand side wire.

While Fig. 2.6 only gives an indication of the ongoing process as a function of

time, the presence of the CTAP process for the counter-intuitively arranged wires can also be inferred from looking at the atomic probability distribution in real space. For this we show in Fig. 2.7 the density of the atomic state in the x and z plane at $t = 0.048$ s integrated over the y -direction. At this time the atomic wavepacket is in the region where the tunnelling interaction between all three waveguides is large and clear differences between the two situations are visible. Fig. 2.7 (a) shows the counter-intuitive situation where the wavepacket can be seen to follow the dark state with only a negligible population component in the middle waveguide. In contrast, Fig. 2.7 (b) shows the intuitive setup, in which the population is distributed between all three waveguides and clear signatures of Rabi oscillations due to the direct tunnelling are clearly visible.

It is exactly these Rabi oscillations in the intuitive process that lead to the time-dependence of the final population in each waveguide and therefore a strong dependence of the outcome on small changes in the system parameters. This can be seen when examining Fig. 2.8, where we show the final population in the right hand side waveguide as a function of the current in the middle wire I_M . For the intuitive process (blue line), the final population varies significantly with changing I_M , whereas the counter-intuitive setup (red line) is very robust to these changes, with the fidelity of population transfer never dropping below 0.98. This is another indication that the transfer is due to CTAP.

From Fig. 2.8 it is also clear that, while there are large oscillations in the fidelity of the intuitive process, there is an upward trend in the fidelity of the process towards unity as the current in the middle wire increases. However, at these higher values of the middle wire current, the waveguides are no longer resonant at all times and one would expect that neither the CTAP nor the intuitive processes would lead to high fidelity transfer. Nevertheless, the simulations show that this is not the case.

We conjecture that in the regime of larger currents in the middle wire the population transfer is due to Stark-shift-chirped rapid-adiabatic-passage (SCRAP) [?]. In this process a time-dependent shift of the energy of the intermediate state in the traditional three-level arrangement allows for high-fidelity population transfer between two states, independent of being in the intuitive or counter-intuitive situation. A translation of this to the spatial realm is straightforward: the approach and retreat of the outer wires from the middle one shift the energy of the central waveguide in a spatially dependent manner. This effect is the topic of a future investigation.

2.5.6 Conclusions

We have performed fully three dimensional simulations of an experimentally realistic waveguide system on an atom chip, where the arrangements of the wires produce spatial dependent tunnel-couplings between the waveguides. These simulations were done by implementing the CUFFT library provided by Nvidia, which made this problem numerically tractable on a desktop computer.

Using a simple method for controlling the resonance as the waveguides are brought close together, we have demonstrated that a counter-intuitive approach of the outer wires to the middle allows to observe high fidelity and robust transfer between the wires due to CTAP. In contrast, for intuitively coupled waveguides, where direct tunnelling between them is allowed to occur, significant Rabi oscillations between all guides exist.

This makes the transfer process highly sensitive to the system parameters. While a large number of theoretical works on CTAP exist, the analysis presented offers a direct way for experimental observation and confirmation of the effect.

Finally, we have also seen a first indication that waveguide systems might be natural systems to observe the SCRAP protocol and a detailed investigation will be the topic of a future work. While we have used the numerical methods described here to perform three dimensional simulations, they can actually be used in any number of dimensions, where they still offer large performance gains over standard CPU approaches.

2.5.7 Acknowledgements

The authors would like to thank Peter Krüger and Thomas Fernholz for valuable discussions and ICHEC for use of their computing resources for the MPI-enabled code. This work was supported by Science Foundation Ireland under project number 10/IN.1/I2979.

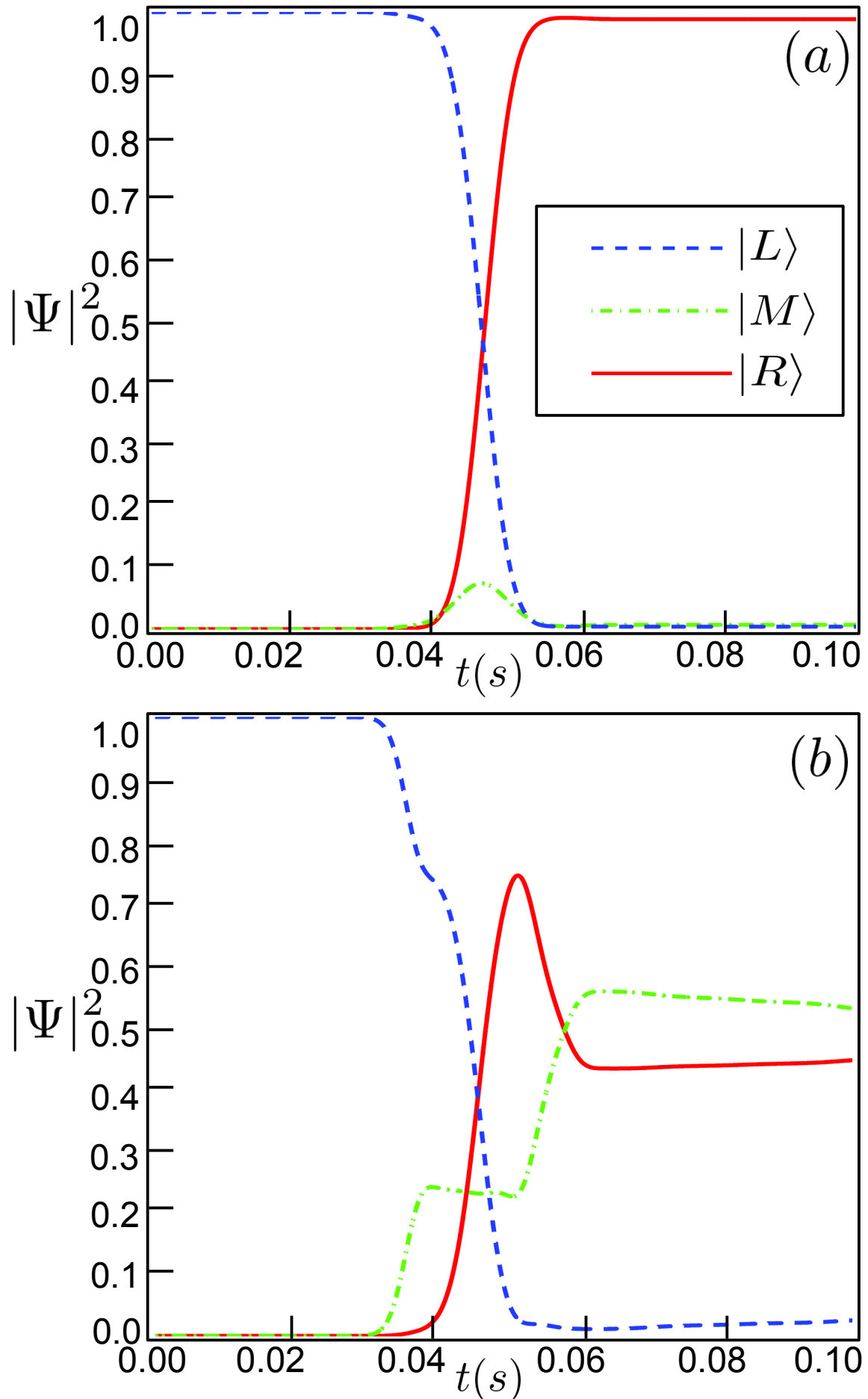


Figure 2.6: (Color online) The population in the left (blue dashed line), middle (green

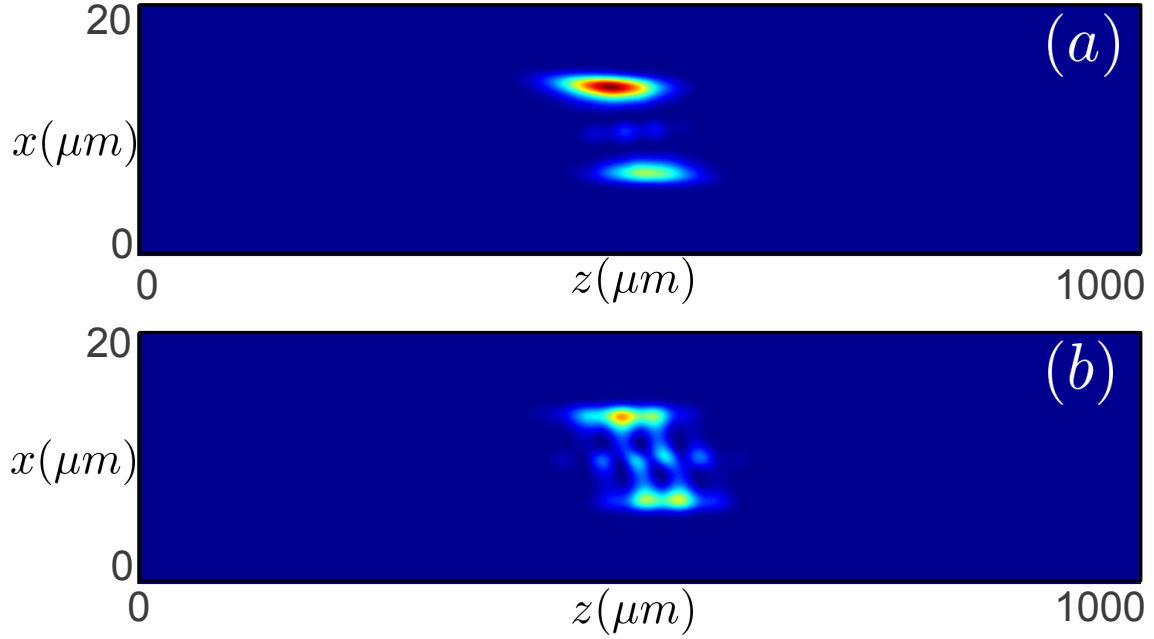


Figure 2.7: (Color online) The density of the atomic state at $t = 0.048$ for (a) the counter-intuitive setup and (b) the intuitive one. The current in the middle wire is $I_M = 0.07$ A in both cases.

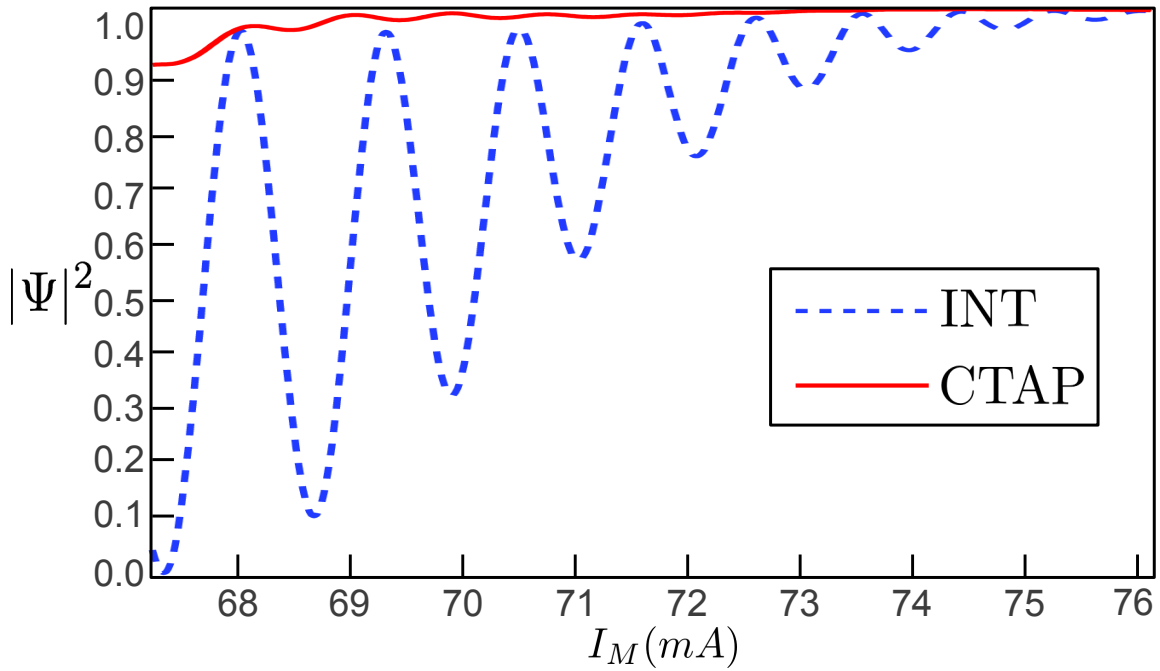


Figure 2.8: (Color online) The final population in the target waveguide for both the CTAP (red solid line) and intuitive (blue dashed line) processes, for values of $I_M = 0.0672$ A to $I_M = 0.0761$ A in steps of 0.001 A.

Chapter 3

Vortex dynamics

3.1 Vortex lattice

Chapter 4

Moiré superlattice structures

4.1 Delta-kick dynamics

The use of delta-kicked Hamiltonians are widespread in the study of chaotic systems [citation]. The delta-kicked rotor is a prime example of such a system that exhibits chaotic motion following a series of successive kicks.

Another such model, building upon the kicked rotor, is the kicked harmonic oscillator, wherein the Hamiltonian acquires an additional quadratic potential. The behaviour of such systems have been studied [], and are interesting to understand the onset of chaos in classical, and quantum mechanical systems. By converting the conjugate variables to quantum operators, the quantum mechanical analogues can be examined. Granted, chaos in the quantum mechanical world differs from that of the classical world (quantum unitary evolution), insights may be gained from the study of systems on the boundary between the quantum and classical world.

Here I propose such a system, given a rapidly Bose-Einstein condensate featuring a well ordered vortex lattice. The goal is to generate chaotic motion of the vortices in the condensate through kicking with an optical lattice that with a period given by the rotation and translational symmetry of the vortex lattice. Since we know the vortex lattice is an Abrikosov lattice with 6-fold symmetry, we can say that given a rotation frequency of Ω , the lattice will return to the same orientation after a rotation of $\Omega/6$. Thus, we can kick the system at this interval with a stationary optical lattice potential, without the need to rotate with the system, making this more experimentally realistic.

We consider a single component Bose-Einstein condensate in a harmonic trap, which in the mean-field limit can be described by the standard Gross-Pitaevskii Hamiltonian

$$H$$

GP = $-\hbar^2 \frac{\nabla^2}{2m} + \frac{1}{2} m \omega^2 \mathbf{r}^2 + g |\Psi(\mathbf{r}, t)|^2$. (4.1) Here ω is the trapping frequency, g describes the strength of the two-particle interaction, and m is the atomic mass. Imposing an external rotation around the z -axis and going into the co-rotating frame leads to a Gross-Pitaevskii equation of the form

$$i\hbar \frac{\partial}{\partial t} \Psi(\mathbf{r}, t) = [H$$

Figure 4.1: (a) Vortex lattice ground-state in a harmonic trap with $\omega_{\perp} = 2\pi \text{ s}^{-1}$ and rotating at $\Omega = 0.995\omega_{\perp}$. This plot shows a condensate with a diameter of approximately $580 \mu\text{m}$; (b) Zoom in of vortex lattice at central density; (c) Optical lattice potential with a periodicity matching that of the vortex lattice.

GP - $\Omega_z L_z \Psi(\mathbf{r}, t)$, (4.2) where Ω_z is the rotation frequency around the z -axis and $L_z = xp_y - yp_x$ is the angular momentum operator. For a rotational frequency close to the transverse trapping frequency, ω_{\perp} , the condensate is known to respond by forming a triangular lattice of vortex lines in the x - y plane [?]. Since we are only interested in the effects stemming from the lattice ordering, we will choose the trapping frequency along the z -axis, ω_z , to be much larger than the one along the transverse axis, ω_{\perp} , so that the condensate assumes a pancake-shaped geometry [?]. This allows us to simplify our analysis by neglecting the z dimension ($\mathbf{r} \equiv [x, y]$), and treat the condensate as a two-dimensional system.

In the following we will solve eq. (4.1) numerically, using a GPU implemented Fourier split operator method [?]. All simulations will use $N = 4.9 \times 10^5$ atoms of ^{87}Rb , which have an s-wave scattering length of $a_s = 4.76 \times 10^{-9} \text{ m}$ [?]. The trapping frequency will be fixed at $\omega_{\perp} = 2\pi \text{ s}^{-1}$, the rotation frequency at $\Omega = 0.995\omega_{\perp}$, and the effective two-dimensional interaction strength is given by

$$g$$

$2d = 4\pi\hbar^2 a_s N \frac{1}{m\sqrt{\frac{m\omega_z}{2\pi\hbar}}} (4.3)$ The numerically calculated ground-state for the above set of parameters is shown in Fig. 4.1 and it can be characterised by the filling factor (or filling fraction) $\nu = N/N_v$, i.e. the ratio of atoms to vortices [?]. For the chosen parameters, the number of vortices within the visible density region is approximately 600, giving a filling factor of $\nu \approx 800$. This places the system within the mean-field quantum Hall regime, and therefore a description using Gross-Pitaevskii theory is adequate [?]. The vortex lattice is highly periodic and the triangular lattice vectors in \mathbf{r} -space are given by $\mathbf{a}_1 = a_v\{1, 0\}$ and $\mathbf{a}_2 = a_v\{-1/2, \sqrt{3}/2\}$, where a_v is the distance between vortex cores. For our analysis we chose to ignore vortices close to the condensate edge, as the distortions in the vortex lattice mean the system can no longer be modelled as a homogeneous arrangement of vortices. The reciprocal (\mathbf{k} -space) lattice vectors corresponding to the given \mathbf{r} -space vectors are $\mathbf{b}_1 = 4\pi/(\sqrt{3}a_v)\{\sqrt{3}/2, 1/2\}$ and $\mathbf{b}_2 = (4\pi/(\sqrt{3}a_v))\{0, 1\}$.

To create a perturbation the condensate is *kicked* by switching on an additional optical potential for a period of time that is much shorter than the rotation period of the Abrikosov lattice ($\tau_{\text{kick}} = 10^{-5} \text{ s}$). The vortex lattice is therefore effectively stationary during the kick. In order to create effects based on periodicity, we chose the optical potential to have the form of a standing lattice, which has the same geometry as the Abrikosov lattice, however not necessarily the same orientation (see Fig. 4.1(c)). To construct such a lattice potential, V_{opt} , we sum counter-propagating laser beams to get

$$V$$

opt = $V_0 \sum_j \cos^2 [\mathbf{k}_j \cdot \mathbf{r}]$, (4.4) where V_0 is the amplitude of the optical lattice potential, and $j = \{0, 1, 2, \dots\}$ is the index of each respective laser with a differing \mathbf{k} -space wave-vector. The triangular structure of the vortex lattice can then be matched by choosing wave-vectors corresponding to the optical potential that follow the vortex lattice vectors $\mathbf{b}_{1,2}$ and adding a third wave-vector with $\mathbf{k}_3 = 4\pi/(\sqrt{3}a_o)\{\sqrt{3}/2, -1/2\}$. Note that these wave-vectors have a lattice constant a_o , which is based on the optical intensity in order to compare with the vortex lattice later. However, as the inter-vortex separation in atomic Bose–Einstein condensates is large, one needs to employ optical lattices with wavelengths on the order of tens of microns [? ?]. For short kicks, and amplitudes on the order of $10^{-2}\mu$, where μ is the chemical potential of the system, the effect of the kick is limited to a phase imprint on the condensates wavefunction [?], which subsequently leads to the development of a flow originating from the position of each maximum of the optical potential. In the following we will show that this in turn leads to well-defined phonon interferences, which, when overlaid on the periodically arranged vortex cores, gives rise to the appearance of moiré super-lattice structures [?] in the condensate density. While in many solid state systems, for example graphene on hexagonal boron nitride [?], the moiré structures are static super-structures, in our case they are dynamical and appear at well defined intervals.

To identify the moiré lattices, we perform a spectral decomposition of the kinetic energy of the condensate [? ? ?]. For this we write the wavefunction in terms of its density, $\rho(\mathbf{r}, t)$, and phase, $S(\mathbf{r}, t)$, as $\Psi(\mathbf{r}, t) = \sqrt{\rho(\mathbf{r}, t)} \exp[iS(\mathbf{r}, t)]$, and obtain from the kinetic energy term in the Gross–Pitaevskii energy functional

$$E$$

kqp = $\int d\mathbf{r} \left(\frac{\hbar^2}{2m} |\nabla \sqrt{\rho(\mathbf{r}, t)}|^2 + \frac{m}{2} |\sqrt{\rho(\mathbf{r}, t)} \mathbf{v}(\mathbf{r}, t)|^2 \right)$. (4.5) The first term in this expression can be interpreted as the quantum pressure term, and the second describes the kinetic energy. We denote the density weighted velocity field as $\mathbf{u}(\mathbf{r}, t) = \sqrt{\rho(\mathbf{r}, t)} \mathbf{v}(\mathbf{r}, t)$, and further decompose it into compressible, $\mathbf{u}^c(\mathbf{r}, t)$, and incompressible, $\mathbf{u}^i(\mathbf{r}, t)$ terms

$$\mathbf{u}(\mathbf{r}, t) = \mathbf{u}^c(\mathbf{r}, t) + \mathbf{u}^i(\mathbf{r}, t), \quad (4.6)$$

defined by $\nabla \times \mathbf{u}^c(\mathbf{r}, t) = 0$, and $\nabla \cdot \mathbf{u}^i(\mathbf{r}, t) = 0$. This decomposition allows the energy contribution from vortex cores (incompressible) and phonon modes (compressible) to be separated [?]. The compressible and incompressible kinetic energy spectra, $E^{c,i}(k)$, are calculated by averaging over shells in \mathbf{k} -space as [?]

$$E^{c,i}(k) = \frac{mk}{2} \sum_{j \in \mathbf{r}} \int_0^{2\pi} d\phi_k \frac{|\mathcal{U}_j^{c,i}(\mathbf{k}, t)|^2}{s_k}, \quad (4.7)$$

where

$$\mathcal{U}_j^{c,i}(\mathbf{k}, t) = \int d^2\mathbf{r} e^{-i(\mathbf{k} \cdot \mathbf{r})} u_j^{c,i}(\mathbf{r}, t). \quad (4.8)$$

Here the $u_j^{c,i}(\mathbf{r}, t)$ are the values of the position-space kinetic energy components in the specified shell, ϕ_k is the polar angle, and s_k represents the number of elements in the chosen shell.

Figure 4.2: Compressible energy spectrum of a non-rotating condensate directly following a kick. A peak at $k = 4\pi/(\sqrt{3}a_o)$ can be seen, which corresponds to the lattice spacing, a_o (indicated by the dashed line), and the smaller, higher energy peaks can be attributed to higher harmonics between nearest and next-nearest neighbours.

Figure 4.3: (a) Main peak of the compressible kinetic energy spectrum for a kicking strength of $V_0 \approx 1.35 \times 10^{-2}\mu$. It can be seen to revive, and eventually disperse over a wide range of wave-numbers. (b) Condensate densities at several times during the evolution. A pattern matching the optical potential can be observed to appear and disappear several times over the course of the evolution.

4.2 Dynamics following a kick

4.2.1 Non-rotating condensate

To understand the effect kicking has on a condensate carrying a vortex lattice, we will first briefly examine the situation where the vortex lattice is absent, i.e. where there is no external rotation. In order to compare this situation with a rapidly rotating condensate, we adjust the trapping frequency in this section such that the background densities match.

For a stationary (non-kicked) condensate the kinetic energy spectrum is constant during time-evolution and a kick leads to the appearance of new, time varying components. To observe this we numerically evolve the system by setting $V(\mathbf{r}, t) = V_{\text{ext}}(\mathbf{r}) + V_{\text{opt}}(\mathbf{r}, t)$, where the time dependent optical potential is only active for $\tau = 10^{-5}$ s of the simulation time, and examine the compressible kinetic energy spectrum following the kick (see Fig. 4.2). Unsurprisingly, the spectrum is dominated by a peak corresponding to the wave-vector associated with the optical potential at $k = 4\pi/(\sqrt{3}a_o)$, and several smaller ones corresponding to its higher harmonics and higher harmonics of next nearest neighbour components of the lattice. As no rotation is created by the imparted phonon modes, the incompressible energy is negligible and we will therefore restrict our analysis to the compressible part of the spectrum.

The evolution of the main peak in the compressible kinetic energy spectrum during the first 250 ms after the kick is shown in Fig. 4.3(a). It initially oscillates in and out of existence and eventually disperses over a wide range of wave-numbers. Snapshots of the density evolution are shown in Fig. 4.3(b), which clearly show that the oscillations correspond to the existence of a transient lattice pattern with several revivals, which has the same underlying structure as the optical potential. In fact, the lattice pattern is best formed whenever the main peak in the kinetic energy spectrum goes to zero, i.e. when the imprinted kinetic energy has been converted into density modulations. The period of the oscillations can be related to the speed of sound divided by the lattice constant and therefore the appearance of the lattice can be attributed to phonon interferences.

Figure 4.4: Condensate density at $t = 1.4 \times 10^{-2}$ s for several optical lattice rotation angles. The cell size of the super-lattice structures can be seen to shrink as the angle is increased. The angles for the examples shown are (a) $\theta_\Delta = 0$, (b) $\theta_\Delta = 2\pi/45$, (c) $\theta_\Delta = 4\pi/45$, (d) $\theta_\Delta = 2\pi/15$.

Figure 4.5: Condensate density after receiving a kick with $\theta_\Delta = \pi/9$. The appearance and disappearance of a moiré structure with wavelength $\lambda_M \approx 2.9a$ over a timescale of about 50 ms can be seen.

4.2.2 Rapidly rotating condensate

Kicking a condensate carrying an Abrikosov vortex lattice with the above optical lattice gives an additional parameter, θ_Δ , which describes the orientation of the imprinted phonon lattice angle relative to the vortex lattice. For simplicity, we assume that the vortex and optical potential lattices have the same lattice constant, $a_v = a_o = a$ (see below for a discussion of the incommensurate case), which means that symmetry allows us to restrict the angle to $\theta_\Delta \in [0, \pi/3]$. We will show in the following that adjusting θ_Δ leads to the appearance of different, transient super-structures in the condensate density.

If $\theta_\Delta = 0$ (see Fig. 4.4(a)) the kicking imparts kinetic energy at wave-numbers that are already well defined in the lattice. This leads to an expansion and contraction of the vortex cores in density only, and no significant change to the compressible kinetic energy spectrum.

However, if the angle between both lattices is finite, super-lattice structures appear after a short time (see Fig. 4.4(b)-(d)), which have a structure cell size that decreases for increasing values of $\theta_\Delta \in [0, \pi/6]$ and increases for larger values until the misalignment angle reaches the lattice symmetry point again at $\theta_\Delta = \pi/3$. These structures are transient and several revivals can be observed before the condensate settles back into the vortex lattice structure with an increase in the background wave-number spread, as expected based on kicking the non-rotating condensate. An example of this for a fixed angle is shown in Fig. 4.5.

To explain the interference patterns observed for misaligning the optical and the vortex lattice, we employ moiré interference theory [?]. Moiré patterns are known to appear when two periodic structures are overlaid while slightly misaligned to each other and can be calculated from the reciprocal lattice vectors. In all generality, any choice of equidistantly separated reciprocal lattice vectors be parameterised as

$$\mathbf{g}_l = g_0 \left[\sin \left(\frac{2\pi l}{\alpha} + \theta \right), \cos \left(\frac{2\pi l}{\alpha} + \theta \right) \right], \quad (4.9)$$

where α describes the rotational symmetry of the lattice, l labels the vector direction on the unit circle, θ is the angle with respect to a chosen coordinate system and g_0 is the reciprocal lattice constant. For our commensurate and triangular lattices we have $g_0 = 4\pi/(\sqrt{3}a)$, $\alpha = 6$ and the vector directions are $l = [0 \dots \alpha - 1]$. As only the relative mis-alignment between the vortex and the phonon lattice matters, we choose $\theta = 0$ for the vortex lattice and $\theta = \theta_\Delta$ for the optical potential alignment. All possible

Figure 4.6: Size of the resulting moiré super-structures as a function of the relative angle between the vortex and optical lattice. The dashed green line indicates the condensate radius. Inset: The different vectors in \mathbf{k} -space of the two lattices, with the optical lattice rotated by an angle θ_Δ . The $\mathbf{g}_{ll'} = |\mathbf{g}_l - \mathbf{g}_{l'}|$ vectors defining the dominant moiré wavelength are those for which the enclosed angle is smallest.

wavelengths that can appear in an interference pattern between two such lattices in real space are then given by

$$\lambda_{ll'} = \frac{\lambda_0}{|\mathbf{g}_{ll'}|}, \quad (4.10)$$

where $\mathbf{g}_{ll'} = \mathbf{g}_l$

V-g_l'^P, and $\lambda_0 = 4\pi/\sqrt{3}$ for our commensurate triangular lattices. One can see from Fig. 4.5 that a pattern matching the longest wavelength, $\lambda_M = \max[\lambda_{ll'}] \approx 2.9a$, appears around $t = 24$ ms and is clearly the most visible one. While patterns with shorter wavelength exist, they are harder to discern in our system and we therefore concentrate on the lowest wave-number in the following.

In \mathbf{k} -space the shortest $|\mathbf{g}_{ll'}|$ corresponds to adjacent wave-vectors with the smallest θ_Δ between them (see inset in Fig. 4.6). Due to the symmetry of the lattices the most visible structures are therefore given by $\lambda_M = \lambda_{00}$ for $\theta_\Delta \in [0, \pi/6]$ and $\lambda_M = \lambda_{01}$ for $\theta_\Delta \in [\pi/6, \pi/3]$ (see inset of Fig. 4.6). While this symmetry assumption no longer holds strictly true after the system has been kicked, it is still fulfilled to a very good approximation during the initial dynamics. We can then obtain the wavelength of the dominating moiré structure as [? ?]

$$\lambda_M = \frac{a}{2 \sin(\eta/2)}, \quad (4.11)$$

where $\eta = \min\{\theta_\Delta, \frac{\pi}{3} - \theta_\Delta\}$ (see Fig. 4.6). These super-structures become observable when the wavelength becomes smaller than the radius of the condensate, which is $\lambda_M \approx 11a$ and which corresponds to an angle $\theta_\Delta \approx \pi/36$. One can see from Fig. 4.6 that once the relative angle is increased beyond this value the structure sizes shrink to a minimum value at the point of complete misalignment, $\theta_\Delta = \pi/6$, giving $\lambda_M \approx 1.93a$, and increase again up to the point of symmetry. Beyond this point the whole behaviour starts over, due to the symmetry of the lattice. Note that in principle the above procedure can be carried out for square or other optical lattice geometries.

The appearance of the moiré vector in k -space can be confirmed from the numerical simulations by looking at the compressible kinetic energy spectra which we display in Fig. 4.7.

Apart from the dominant peaks corresponding to the underlying triangular geometry of the Abrikosov lattice, which are independent of θ_Δ (straight lines in Fig. 4.7), a number of additional peaks appear. Their position is a function of the misalignment angle and the lowest wave-number that appears increases its value with increasing Δ_θ . This is consistent with the moiré model and the appearance of density structures of differing size. Furthermore, a symmetric repeat of this structure about the $\theta_\Delta = \pi/6$ point is also visible, which corresponds to the $\pi/3 - \theta_\Delta$ lattice vector component. The minimum wavelength observed agrees with the theoretically determined minimum

Figure 4.7: Compressible kinetic energy spectrum as a function of θ_Δ . All values are time-averaged over an interval $t = 0$ s to $t = 1$ s. The moiré peak corresponding to the lowest wave-number can be seen shifting to larger values for increasing angles and similar behavior is visible for the higher order components.

Figure 4.8: (a) For a kicking strength of $V_0 = 5.4 \times 10^{-2}\mu$ for a non-rotating condensate higher order modes become non-negligible contributions to the compressible kinetic energy spectrum. This leads to a variety of different density structures, with some close-ups shown for (b) 24 ms, (c) 36 ms, (d) 56 ms, and (e) 88 ms. Note that the larger structures in these plots are given by the optical lattice constant, which sets the scale.

value of $\lambda_M \approx 1.93a$ and all other values over the range of observed angles. Note that for the higher harmonics at larger wave-numbers similar behaviour exists and is also covered by the moiré model.

Let us briefly discuss what happens for stronger kicking, or when the two lattices are non-commensurate. In the above the strength of the kicking pulse was chosen such that its perturbation only leads to a phase imprinting [? ?], with minimal change to the initial density. If one increases the kicking intensity the situation becomes quite different and one can see from Fig. 4.8(a) that higher order wave-numbers become more strongly excited. This, in turn, leads to modulations of the condensate density at shorter wavelength and an example is shown in Figs. 4.8(b)-(e). However, as for fully realistic experimental situations it is necessary to consider the heating of the condensates due to the disturbance once the kicking becomes stronger, we restrict this investigation to low intensity pulses.

A situation where the optical and the vortex lattice have different lattice constants can be imagined to appear naturally due to experimental uncertainties. Defining $a_o = a_v(1 + \epsilon)$ the expression in eq. (4.10) can be calculated to be

$$\lambda_M = \frac{a_v(1 + \epsilon)}{\sqrt{2(1 + \epsilon)(1 - \cos \theta) + \epsilon^2}} \quad (4.12)$$

which reduces to eq. (4.11) for $\epsilon = 0$. Evaluating this expression shows that the largest moiré wavelength changes slightly for small values of ϵ , but it remains distinct enough from the underlying wave-vectors to stay visible in the evolution. This ensures that the system examined here is experimentally realistic.

4.3 Kinetic energy decomposition

4.4 Superlattice structures

4.5 Moiré interference theory

Chapter 5

Defect engineering

5.0.1 Rapidly rotating BEC

For this work, we numerically solve the Gross-Pitaevskii equation in two dimensions, assuming a strong confinement along the third axis. This allows all dynamics to be restricted to the xy plane, with vortices behaving as charged particles in a neutral background. In the frame corotating with the condensate, this can be modeled as

$$i\hbar\partial_t\Psi(\mathbf{x},t) = \left[-\frac{\hbar^2}{2m}\nabla^2 + V(\mathbf{x}) + g|\Psi(\mathbf{x},t)|^2 - \Omega L_z \right] \Psi(\mathbf{x},t) \quad (5.1)$$

where $V(\mathbf{x})$ is the trapping geometry, Ω is the trap rotation frequency, and L_z is the angular momentum operator along the z -direction. For the rapidly rotating case, the vortices form an ordered triangular lattice, that rotates equivalently to a solid-body in the large number limit. Deviations from the solid-body rotation can be seen for trajectories in the limit of long times (> 10 s). This is very likely due to long-wavelength Tkachenko modes in the condensate, and following the analysis of [Baym, Tk modes of vtx latt in rr BEC] has a frequency much longer than the lifetime of the system for our given rotation rate. The lattice is well ordered and behaved at timescales on the order of upto few seconds, as well as away from the condensate edges, and so we will restrict our analysis therein.

As condensates are highly controllable in the lab (cite many papers), we consider the use of many common experimental techniques to engineer specific states otherwise difficult in solid-state materials. One such set of systems are those of crystals with controllable defects, which although (relatively) easily created classically (cite bead packing, etc), are difficult experimentally in quantum systems due to the sizes of interatomic spacings. Here we propose the use of phase-imprinting (cite) as a means of achieving such defects in a Bose-Einstein condensate. Through direct manipulation of the condensate phase, vortices may be added or removed from specific locations in the system.

5.0.2 Order/disorder

Given the localised defect disturbs the lattice after sufficiently long times, we can examine if the lattice moves from global ordered to disordered following the addition

or removal of another site over the course of time. For a two-dimensional material, KTHNY theory describes the transitions from a solid crystalline to amorphous fluid phase, via an intermediate hexatic phase. This state is generally characterised by the translational and orientational correlation functions long-ranged behaviour. As we have an inhomogeneous density profile, and thus lattice outside a given radius, the use of translational correlations does not make much sense. Orientational correlations however, which measure how the lattice aligns to a particular angle, should suffice when combined with the density structure factor, $S = \int d\mathbf{r} e^{i\mathbf{k}\cdot\mathbf{r}} |\Psi|^2$. True crystalline behaviour is given by orientational constant values, with power-law decay is expected for a hexatic phase, and exponential decay for an amorphous fluid (neglecting translational correlations).

5.0.3 Phase imprinting defects

Phase imprinting has been shown as an effective tool for the creation of vortices within a Bose-Einstein condensate (cite). The signature of a quantum vortex is given by a phase singularity, around which the phase winds through $\pm 2\pi$, depending upon the direction of rotation. Through the use of the phase imprinting method, we can eliminate a vortex from the lattice by applying the correct phase profile. To eliminate a vortex from the lattice we need only to apply the opposite phase winding to that of the vortex to be eliminated. The instantaneous application of a phase singularity to the condensate will create phonon modes in the density, as will the annihilation event. Since the induced phonons have been shown to yield minimal impact on the vortex lattice structure <ref my paper>, we can safely ignore their contribution. The removal of a vortex from the lattice introduces a vacancy to the system.

We model the vortex lattice as a graph, where each vortex represents a node, and edges are given by nearest neighbours at most separated by a distance a_0 , for a triangular lattice configuration, or $\sqrt{2}a_0$ for a square lattice (see Fig. ??). The inclusion of the square lattice distance is chosen so that upon removal, the vortices can reconfigure their arrangement locally, and may move from triangular to square geometries. As they behave like Coulombic particles with a profile that falls off as r^{-1} we can consider that any interactions outside these distances to be negligible.

Lattice vacancy

The removal of a vortex from the vortex is thus expected to affect only the nearest neighbours by altering their velocity well, with the overall angular momentum of the condensate decremented by a single quantum. The resulting vacancy, following a vortex removal, remains localised to its respective position within the lattice for long times, regardless of initial placement (assuming not at edge) (see Fig. ??). The resulting stability of the nearest neighbours follows a decay of the honeycomb-like structure akin to that described by [statistical topology of perturbed two-dimensional lattices]. Given enough time, this structure decays via one of the three possible means, creating a locally disordered region with a grain boundary/disclination/dislocation? evident of the lattice change. However, even for long times, the overall vortex lattice remains well structured, as evidenced by examining correlation functions of the vortex positions for

Figure 5.1: (top) Doubly charged central vortex. Doubly charged vortex remains stable, and retains 6-fold symmetry of vortex lattice. (bottom) Doubly charged central vortex, and removal of nearby vortex. Doubly charged vortex remains stable, and forms 8-fold symmetry of vortex neighbours.

both two-body, and orientational correlations.

After the vortex removal, the system remains in a stable configuration, for a period on the order of 100+ ms (see Fig. ??, ??), after which the vortices begin to deviate from their lattice positions and attempt to fill the vacancy and balance the inter-vortex forces. Removing vortices at different positions in the lattice shows similar behaviour, with the effect on the velocity profile and trajectories of other vortices being mostly localised around the removal site.

Tracking the vortex distances traveled for different removal locations, and for a different number of removed vortices shows how much we disturb the underlying lattice (see ??).

Lattice overpopulation

Similarly to removing a vortex from the lattice, we can also add one. By choosing a pre-existing vortex and adding a like-signed phase winding, we can create multiply charged vortices in the condensate, where the vortex has a winding of $2\pi l$, with l as the vortex charge. Multiply charged vortices are usually unstable in condensates, as it is more energetically favourable to have two singly charged vortices, than a single doubly charged vortex, as the energy increases with l^2 . Thus, an l -charged vortex is expected to instead decay into l singly-charged vortices.

Here we have taken our lattice of $l = 1$ vortices, and given an additional charge to a single vortex to examine the decay process. However, the presence of the lattice suppresses the decay process for long times (order of seconds) compared to that of in a condensate without vortex lattice. The doubly charged vortex remains stable on the order of seconds even away from the lattice centre (though does decay eventually). The additional velocity profile locally causes the nearest neighbouring vortices to rotate faster than the solid-body rotation rate of the whole lattice, causing a local shearing of the lattice structure. As with the vacancies, the use of correlation functions allowed us to examine the short and long-range order of the lattice.

Voronoi diagrams of the resulting lattice show a stable doubly charged vortex position, with show twisting of the lattice about this central point.

5.0.4 Things to note

- Localised disturbances: introducing vacancy to lattice causes it to travel with lattice. Change in velocity profile only affects 6 nearest neighbours on moderate timescales.
- Long range hexatic phase has short range translational order (exp drop off), but constant orientational order -> is this such a phase?

5.0.5 Correlations

According to KTHNY theory for a 2D material the transition from a solid crystal to liquid phase is mediated through an intermediary hexatic phase. This phase is usually characterised by the translational and orientational correlation functions. Given the lack of translation order in a harmonically trapped condensate, we restrict our analysis to the orientational correlation function, g_6 given by

$$g_6(r) = \frac{1}{N(r)} \sum_{i,j}^{N(r)} \psi_6(\mathbf{r}_i) \psi_6^*(\mathbf{r}_j), \quad (5.2)$$

with

$$\psi_6(|\mathbf{r}_i - \mathbf{r}_j|) = \frac{1}{n_i} \sum_j^{n_i} \exp(6i(\theta_i - \theta_j)), \quad (5.3)$$

where ψ_6 is the orientational order parameter, and j is over the nearest neighbouring vortices.

According to [] the decay in correlations for both translational and orientational order give indication to the material phase. In a two-dimensional material the positional order is expected to decay algebraically as a function of radius, differing from that of a three-dimensional material, which tends to a constant value. Here we examine the orientational correlation function as a measure of the order of a "vortex unit cell", consisting of the angle made by nearest neighbours to an individual vortex. For a perfectly ordered triangular lattice this value will tend to 1. To maintain constant vortex areal density, we choose vortices defined at a radius of $r = 2 \times 10^4$ m from the centre, which give an almost uniform lattice constant for our system parameters.

- Crystalline: $\lim_{r \rightarrow \infty} \hat{g}_T(r) \neq 0$, $\lim_{r \rightarrow \infty} \hat{g}_6(r) \neq 0$
- Long-range hexatic: $\hat{g}_T(r) \approx_{r \rightarrow \infty} \exp(-r/\xi_T)$, $\lim_{r \rightarrow \infty} \hat{g}_6(r) \neq 0$
- Power-law hexatic: $\hat{g}_T(r) \approx_{r \rightarrow \infty} \exp(-r/\xi_T)$, $\hat{g}_6(r) \approx_{r \rightarrow \infty} 1/r^{\eta_6}$
- Amorphous: $\hat{g}_T(r) \approx_{r \rightarrow \infty} \exp(-r/\xi_T)$, $\hat{g}_6(r) \approx_{r \rightarrow \infty} \exp(-r/\xi_6)$

Hat means normalised (see page 119 of order in two dim binary random arrays, Nelson et al.)

5.0.6 Numerics and results

Each vortex position was found by summing over adjacent grid sites, and looking for a 2π phase winding. This gave a vortex position estimated to the numerical grid. A least-squares fit was performed to more accurately determine the vortex core. Vortices closest the centre of the condensate were considered to ensure an almost uniform inter-vortex spacing, giving minimal deviation in lattice constant, a_0 . Each vortex was assigned a unique identifier (UID) to allow for it to be tracked individually over the course of the simulations, with the initial configuration presented in the graph [ref graph]. By

noting these UIDs, vortices can be individually selected for removal by applying the global 2π phase winding in the opposing direction, centered on the core.

The trajectory plots show very small global effect on the core positions, with a disturbance localised in a region centered on the removed core. By removing vortices in different locations on the condensate we see similar behaviour, with the trajectories modified in a region around the removed vortex. The removal of two vortex adjacent cores can be seen to create a greater disturbance, as expected, with the trajectories of the surrounding vortices no longer following an almost circular path (more like hexagonal), but taking on other geometric path shapes. For two nn vortices the path becomes an almost rhombic shape, with nnn forming an elongated hexagon (as to be expected). For 3 nn, the resulting trajectories follow a triangular pattern of the same orientation as the removed vortices. For the removal of an entire 7 vortex cell, the formed pattern is star shaped.

TODO: Calculate incompressible kinetic energy spectrum for each case, and see if useful. RESULT: It wasn't. Calculate $S(k) = |\Psi(k)|^2$ for condensate densities, not just vortex positions, for comparison. RESULT: looks strange, even in untouched case. Arcs exist in all cases, but with interference lines.

The impact on the overall distances traveled by each vortex as a result of the dislocations is given in figure [some fig].

Conclusion

This is the conclusion. You might want to leave it unnumbered, as it is now. If you want to number it, treat it like any other chapter.

Appendix A

Appendices and Supplementary Data

Unlike a journal article, no data or discussion may be presented separately as unpublished supplementary documents or data. Appendices should be used instead for material that is tangentially relevant to the thesis but does not fit in the main narrative. If you need to refer to large volumes of data that cannot be printed (such as an annotated genome, or a simulation with moving images), lodge the data on an OIST repository or a public database and provide the URL of the dataset in the thesis.

Bibliography